Characterization of Polarization in Large Diameter Periodic Lattice Plasmonic Nanolasers

Charles Rambo

Master thesis

April 2021

Department of Physics and Mathematics
University of Eastern Finland

Charles Rambo *Characterization of Polarization in Large Diameter Periodic Lattice Plasmonic Nanolasers*, 58 pages
University of Eastern Finland
Master's Degree Programme in Photonics

Supervisors Assoc. Prof. Tommi Hakala
MSc. Janne Heikkinen

Abstract

Plasmonic nanolasers relying on the excitation of localized surface plasmons in a lattice represent a promising solution to the challenges of developing nanoscale lasers which have both a smaller footprint and lower power consumption than conventional lasers. Here, the lasing capabilities of seven structures of square periodic gold particle lattices utilizing IR 792 laser dye and femtosecond pumping are examined using spectroscopy and interferometry in the real and k-spaces with a focus on polarization. Spatial coherence was observed for all cases in both the near and far field. The lattices were all found to produce fields similar to the LG_{00} and LG_{01} modes. A transition point between the dominance of these two modes was established to between a particle diameter of 170 nm to 180 nm. Where measurable, the LG_{00} mode was found to have a degree of linear polarization greater than 0.974. The LG_{01} mode was used to identify the bound in continuum state in all arrays as TE-1.

Keywords: Plasmonics(250.5403); Interferometry(120.3180); Nanophotonics and Photonic Crystals(350.4238); Coherence(030.1640); Fourier optics(070.0070); Polarization(260.5430)

Preface

Dedicated to George. There will likely be other Georges after you but you have been by far the Georgeiest. I thank you for taking care of my family while I have been on this adventure, and I will never be able to thank my family enough for taking care of you. And of course to Dad, Mom, and Aaron. A special debt of gratitude goes to all of the educators who have inspired me over the years, with the completion of this work I am one step closer to repaying what you have given me.

Joensuu, April 30, 2021

Charles Rambo

Chapter I

Introduction

It would be impossible to deny that lasers have been one of the most important inventions since the first one was built just over sixty years ago. If it is not their direct use in enabling high-speed communication and manufacturing, their importance to research is incalculable. Many of these applications demand that physical size and power consumption are minimized. This has been a driving force behind the development of nanolasers in general with such devices that produce lasing by taking advantage of plasmons referred to as plasmonic nanolasers. Rapid development of the plasmonic nanolaser has been seen since this technology was first demonstrated in 2009 [1]. This thesis surrounds investigations into the lasing capabilities of a plasmonic nanolaser with square periodic gold nanoparticle arrays on a glass substrate immersed in IR 792 laser dye, focusing on polarization and the effect of changes to the particle diameter.

Applications for lasers that consume less energy and take up less space are not insignificant; three specific areas where nanolasers have shown particular promise are telecommunications, near field spectroscopy and sensing, and biocompatible sensors. In telecommunication, they can lower the power per bit consumption [2] and the suitability for direct waveguide integration [3] make them excellent candidates for the next generation of optical interconnects [1]. Refractive index sensing [4], and cell labeling/tracking are just a couple of the demonstrated biological uses.

A particularly exciting development in nanolasers has been lasing of the dark mode which has many of its own applications. The dark modes are subradiant and have a much higher quality factor (Q), but it has been a challenge to couple them to the far field. [5]. A dark mode appears in the far field as a toroid. These

doughnut shaped fields go by a variety of names, but are noted for having the ability to carry orbital angular momentum [6]. These include but are by no means limited to imaging, metrology [7], optical manipulation [2] and quantum computing [8].

One sign of the possibilities that exist in the research of plasmonic nanolasers is the wide variety of structures that are being explored. A range of different lattice geometries have been used including triangular/hexagonal [9] and even aperiodic [10]. Even more have been proposed, including rectangular, oblique, and rhombic lattices [11]. Copper [12] and silver [5] have been experimented with as well. Additionally, the use of different dyes is a particularly active area of research in this field [13, 14].

A common analysis of systems utilizing periodic plasmonic nanostructures, such as the nanolaser investigated here is to image the k-space of the field that is generated when the array is excited. One of the earliest examples of this is the work of Kravets et al. [15–24]. The reason for the intense focus on the k-space is that a key feature of conventional lasers is their limited divergence. Imaging the k-space informs on how the beam will appear in the far field. Following this path, the k-space is investigated both directly and using interferometry under varying polarization. The results are analyzed independently and are then compared to measurements of the real space.

The key results of these studies were that large-diameter particle arrays were examined for the first time, and all demonstrated lasing capabilities. Importantly a transition from the bright mode regime to the dark mode regime was found to occur somewhere between arrays with 170 nm and 1780 nm particles, and further, that the intensity of the bright mode grows exponentially with particle diameter. When the bright mode is dominant, it is seen to be highly linearly polarized with a degree of linear polarization between 0.974 and 0.999. k-space measurements were used to identify the bound states in continuum in all the measured arrays to be TE-1. Finally, wavefront folding interferometry revealed coherence in both the near and far fields, which helped to demonstrate the evolution of both the bright and dark modes.

In the next chapter, the theories key to the measuring and functioning of the nanolaser will be discussed. The following chapter will describe the experimental setup and how it was utilized for data collection. The third chapter presents the data and analyzes what results can be taken from the measurements before conclusions are given in the final chapter.

Chapter II

Theoretical Background of Methods & Plasmonic Lasers

The lasing capabilities of this system are primarily evaluated in the k-space. The first section of this chapter will be a brief survey of Fourier optics. The next section is focused on the properties of lasers, and specifically the properties which will be investigated here. Finally, the workings of the plasmonic nanolaser evaluated in this thesis are laid out, including special consideration of plasmon theory.

2.1 Fourier Optics

The Fourier transform is a valuable tool to both mathematicians and physicists. It is built on the concept that any periodic function may be expressed as a sum of periodic functions, namely, sine and cosine. Further, through windowing, any function may be adjusted to be periodic such that the Fourier transform can act on it. In one dimension the Fourier transform of an arbitrary function f is given by

$$f(x) = \frac{1}{\pi}\left[\int_0^\infty A(k)\cos kx dk + \int_0^\infty B(k)\sin kx dk\right]. \tag{2.1}$$

Where, with x' serving as a placeholder value,

$$\begin{aligned} A(k) &= \int_{-\infty}^{\infty} f(x')\cos kx' dx' \\ B(k) &= \int_{-\infty}^{\infty} f(x')\sin kx' dx'. \end{aligned} \tag{2.2}$$

By substitution and application of Euler's formula, it is possible to arrive at the Fourier transform pair:

$$\begin{aligned} f(x) &= \frac{1}{2\pi} \int_{-\infty}^{\infty} F(k) e^{-jkx} dk \\ F(k) &= \int_{-\infty}^{\infty} f(x) e^{jkx} dx. \end{aligned} \tag{2.3}$$

This pair of equations may easily be generalized to higher dimensions such as the two-dimensional form

$$\begin{aligned} f(x,y) &= \frac{1}{(2\pi)^2} \iint_{-\infty}^{\infty} F(k_x, k_y) e^{-j(k_x x + k_y y)} dk_x dk_y \\ F(k_x, k_y) &= \iint_{-\infty}^{\infty} f(x,y) e^{j(k_x x + k_y y)} dx dy, \end{aligned} \tag{2.4}$$

or even the time (t) and angular temporal frequency domain (ω)

$$\begin{aligned} f(t) &= \frac{1}{2\pi} \int_{-\infty}^{\infty} F(\omega) e^{-j\omega t} d\omega \\ F(\omega) &= \int_{-\infty}^{\infty} f(t) e^{j\omega t} dt. \end{aligned} \tag{2.5}$$

Both Eqns. 2.4 and 2.5 will be used in this work. Using the standard script 'F' ($\mathcal{F}$) to denote the transform, this sets up a series of relations between the function f and its transform and the inverse of its transform ($\mathcal{F}^{-1}$).

$$f(x) = \mathcal{F}^{-1}\{F(k)\} = \mathcal{F}^{-1}\{\mathcal{F}\{f(x)\}\} \tag{2.6}$$

$$F(k) = \mathcal{F}\{f(x)\} \tag{2.7}$$

$$\mathcal{F}\{F(k)\} = 2\pi f(-x) \tag{2.8}$$

A common use of the Fourier transform is to perform harmonic analysis on a function, such as a signal, to discover the frequencies that are constituent to the function. There are also other physical interpretations for the transform. For

instance, when a plane wave arrives at a small angle to a thin lens, the wave will be focused to a point on the back focal plane of the lens as shown in Fig. 2.1. In fact, for any small angle wave incident on the lens, it will be focused to a point based on the angle it arrived. The lens in this system may be referred to as a Fourier lens,

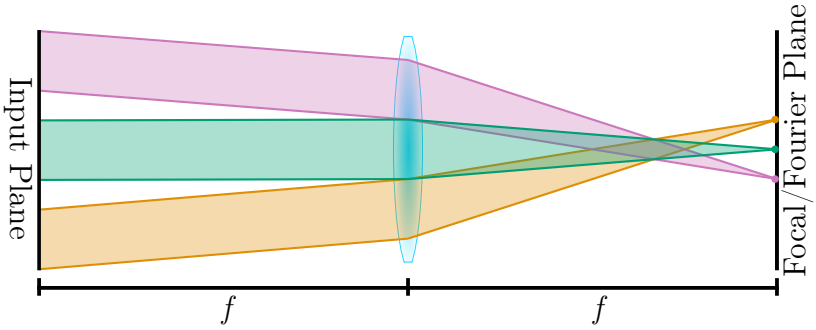

Figure 2.1: According to Fourier optics, a lens performs the Fourier transform on the field by collecting all parts of the field which are propagating at the same angle to the lens to a single point. Thus giving the shape, and in turn the k-space image, of the field [25].

and the back focal field is the Fourier plane [26]. This is because it is taking the two-dimensional Fourier transform of the front focal or input plane. As a confidence check, now assume that the back focal plane of the case shown is used as the front focal field of another Fourier lens. One would expect that the image would appear as it did at the start, but flipped just as Eqn. 2.8 predicts. Because the initial field is now a function of k, this will often be referred to as the k-space [27]. Aside from the angular temporal frequency, there are a few other ways to interpret what measurement of the k-space reveals. It is also giving the angular beam profile (shape of the beam) [28], as well as allowing the far field to be imaged over a much smaller distance [25].

2.2 Characteristics of a Laser

The standard for laser setup is to have some sort of matter (called the gain medium) inside a mirror cavity. The system will then have energy added to it in an action called pumping. The pumping may be either electrical or optical and will cause excitations in the matter as it absorbs energy. The matter will eventually release this energy in the form of a spontaneous emission. The spontaneous emission will

stimulate other emissions from the excited gain medium leading to more excitations and emissions. The released energy does not necessarily have to be in the form of light, but ideally, the pump energy and the emitted energy will work together to cause a predictable flow of photons. The gain medium may be atoms or molecules of a liquid, solid, or gas. Whiskey [29], Thulium [30], Helium-Neon [31] may serve as respective examples. Likewise, there are a plethora of options for the construction of the cavity, but it is generally desirable to have a wall of the cavity that is as reflective as possible to the wavelength of the emissions and another wall that is slightly less reflective. The shape of the cavity will also affect its ability to induce lasing. As it was stated in the introduction that a benefit of the plasmonic nanolaser is its size, it is worth mentioning here that the cavity is one of the key limitations of conventional lasers. A key restriction on the length (L) of the cavity is it must be able to host the laser modes as

$$L = \frac{\lambda_0}{2n} m \tag{2.9}$$

where λ_0 is the free space wavelength of the mode, n is the refractive index, and m is an integer. Directly this gives a minimum cavity length of half the wavelength [32]. If all conditions are met, a beam with certain desirable properties is emitted from the system. These properties include monochromaticity (few wavelengths in the beam), coherence (positions in time or space where the beam is consistent), directionality, and high intensity. Often, but not always, short time duration is added to this list [1, 31]. The study of coherence as well as polarization are crucial to this work and need to be considered further.

2.2.1 Coherence

Coherence may be thought of as the degree of how constant the phase of a field is. Often, it is convenient to treat a field as being fully coherent or incoherent, but in actuality, all wave phenomena will sit somewhere between these two as partially coherent. Coherence is a highly active area of research and any thorough investigation would likely be worthy of a thesis of its own. Broadly speaking, coherence considers the spatial and temporal similarities of a wave with itself which are generally referred to as spatial and temporal coherence. There are, however, disagreements between authors of key texts as to the nature of this nomenclature. Some say that

spatial coherence and temporal coherence are one and the same; calling the distinction artificial [25], others say they are fully independent [31], and others do not use the terms at all [33]. Regardless, temporal coherence correlates to the bandwidth of a source and is more or less how little the field morphs in time. The correlation function $\mathbf{\Gamma}$ for the point $\mathbf{r}$ in some field at two points separated by time τ is given by

$$\mathbf{\Gamma}(\mathbf{r},\tau) = \lim_{T\to\infty}\frac{1}{T}\int_0^\infty \mathbf{E}(\mathbf{r},t+\tau)\mathbf{E}^*(\mathbf{r},t)dt = \langle \mathbf{E}(\mathbf{r},t+\tau)\mathbf{E}^*(\mathbf{r},t)\rangle, \tag{2.10}$$

where the angle brackets represent the averaging of an ensemble of measurements over time. This may be normalized to give the complex degree of temporal coherence γ as

$$\gamma = \frac{\langle \mathbf{E}(\mathbf{r},t+\tau)\mathbf{E}^*(\mathbf{r},t)\rangle}{\left(\langle \mathbf{E}(\mathbf{r},t)\mathbf{E}^*(\mathbf{r},t)\rangle\langle \mathbf{E}(\mathbf{r},t+\tau)\mathbf{E}^*(\mathbf{r},t+\tau)\rangle\right)^{1/2}}. \tag{2.11}$$

Finding the simple degree of temporal coherence is simply a matter of finding the magnitude ($|\gamma|$). Having been normalized to one in Eqn. 2.11, it follows from the Cauchy–Shwartz inequality ($|\langle \mathbf{u},\mathbf{v}\rangle| \leq \|\mathbf{u}\|\|\mathbf{v}\|$) that the degree of temporal coherence is also normalized to one [31]. Similarly, it is possible to quantify how similar two points on the wavefront are with temporal coherence as

$$\mathbf{\Gamma}(\mathbf{r}_1,\mathbf{r}_2,0) = \lim_{T\to\infty}\frac{1}{T}\int_0^\infty \mathbf{E}(\mathbf{r},t)\mathbf{E}^*(\mathbf{r},t)dt = \langle \mathbf{E}(\mathbf{r}_1,t)\mathbf{E}^*(\mathbf{r}_2,t)\rangle, \tag{2.12}$$

$$\gamma = \frac{\langle \mathbf{E}(\mathbf{r}_1,t)\mathbf{E}^*(\mathbf{r}_2,t)\rangle}{\left(\langle \mathbf{E}(\mathbf{r}_1,t)\mathbf{E}^*(\mathbf{r}_1,t)\rangle\langle \mathbf{E}(\mathbf{r}_2,t)\mathbf{E}^*(\mathbf{r}_2,t)\rangle\right)^{1/2}}. \tag{2.13}$$

Again, the absolute value of the complex degree of temporal coherence gives the degree of spatial coherence ($|\gamma|$), and both values are normalized to one. Importantly, as it is not physically realizable to have zero path difference (and therefore no time difference), temporal and spatial coherence may be generalized to

$$\mathbf{\Gamma}(\mathbf{r}_1,\mathbf{r}_2,\tau) = \lim_{T\to\infty}\frac{1}{T}\int_0^\infty \mathbf{E}(\mathbf{r}_1,t+\tau)\mathbf{E}^*(\mathbf{r}_2,t)dt = \langle \mathbf{E}(\mathbf{r}_1,t+\tau)\mathbf{E}^*(\mathbf{r}_2,t)\rangle, \tag{2.14}$$

and

$$\gamma = \frac{\langle \mathbf{E}(\mathbf{r}_1,t+\tau)\mathbf{E}^*(\mathbf{r}_2,t)\rangle}{\left(\langle \mathbf{E}(\mathbf{r}_1,t)\mathbf{E}^*(\mathbf{r}_1,t)\rangle\langle \mathbf{E}(\mathbf{r}_2,t)\mathbf{E}^*(\mathbf{r}_2,t)\rangle\right)^{1/2}}, \tag{2.15}$$

which gives the mutual coherence function, and the complex degree of coherence, respectively. The degree of coherence will then be

$$|\gamma(\tau)| = \gamma(\tau) \exp j \left[\phi(\tau) - \langle\omega\rangle\tau\right]. \tag{2.16}$$

When two coherent fields interact, they will generate an interference pattern of high and low intensities called fringes. To this end, coherence is a measure of how well two points, either in time or space, will interfere with each other. The visibility V of the fringes that (may or may not) appear are then a convenient way to quantify coherence as

$$V(\tau) = \frac{I_{\max} - I_{\min}}{I_{\max} + I_{\min}} = \left|\gamma(\mathbf{r}_1, \mathbf{r}_2, \tau)\right|, \tag{2.17}$$

where I_max is the intensity of a bright peak where there is constructive interference, and I_min is a dark trough where there has been destructive interference.

Measurement of Spatial Coherence

All of the interferometry measurements in this thesis have been collected with a path difference of approximately zero, meaning that they are principally a measurement of spatial coherence. Traditionally, the measurement of spatial coherence has been done using Young's double-slit or double-pinhole interferometer. Fig. 2.2a illustrates this type of interferometer being used to find the spatial coherence of the field $\mathbf{E}$ at x and $-x$. The field at each point arrives at the holes which cause spherical waves to be formed. An interference fringe pattern will appear on the screen or may be recorded by the detector. In the paraxial case, this pattern will resemble the cosine function as illustrated (in the non-paraxial case the pattern will follow sinc^2). As discussed previously, the spatial coherence of the field is then a matter of how visible the fringes are. if $\mathbf{E}(x)$, and $\mathbf{E}(-x)$ are not at all coherent, the fringes will not appear. When the coherence is at a maximum the intensity at the screen will alternate from the sum intensity of the two fields to zero. While this type of interferometer is indeed simple, to measure the full spatial coherence of the field, all possible points must be compared, which requires changing the position of the pinholes and remeasuring. The wavefront folding interferometer (WFI) is then be seen as an upgrade to Young's interferometer. An early description gives one construction of the WFI as resembling the Michelson interferometer where the mirror on one arm has been replaced with a rooftop mirror [34] as shown in Fig.

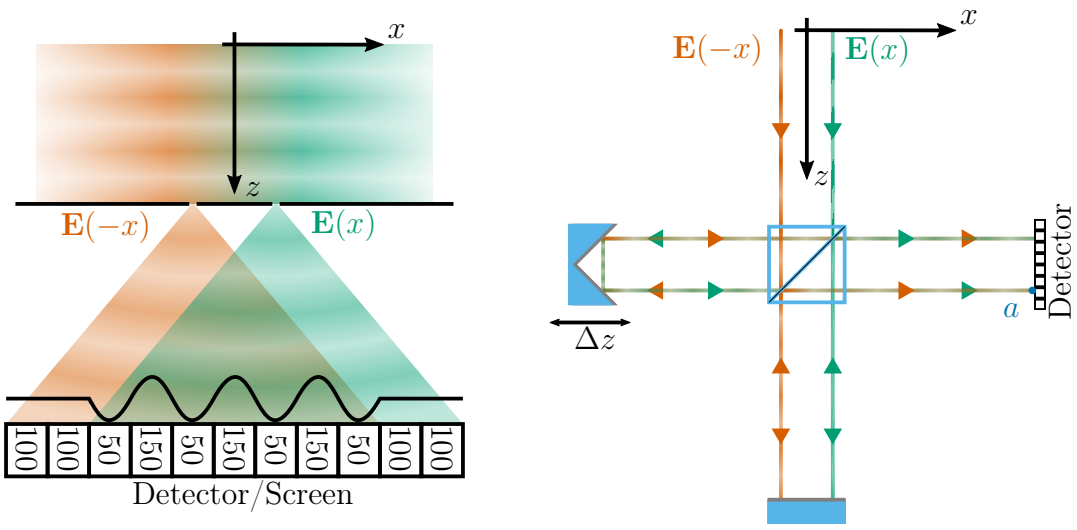

(a) (b)

Figure 2.2: Two interferometers commonly used for measuring spatial coherence. (a) Young's double-pinhole interferometer with an example detector measuring arbitrary units. (b) A scanning wavefront folding interferometer demonstrating the path that each half of the field takes.

2.2b. The field entering the interferometer at any point x will be divided by the beam splitter. Using the convention in Fig. 2.2, half of the field will be flipped such that at the detector the field at an arbitrary point a will be

$$\mathbf{E}_a = \frac{1}{\sqrt{2}}\mathbf{E}(x) + \frac{1}{\sqrt{2}}e^{i\Delta}\mathbf{E}(-x). \tag{2.18}$$

Of course, the detector will actually measure the intensity of this field as some time average as

$$\begin{aligned} I_a = \langle \mathbf{E}_a \cdot \mathbf{E}_a^* \rangle &= \frac{1}{2}\left[I(x) + \langle e^{i\phi}\mathbf{E}^*(x)\mathbf{E}(-x)\rangle + \langle e^{i\phi}\mathbf{E}(x)\mathbf{E}^*(-x)\rangle + I(-x)\right] \\ &= \frac{1}{2}\left[I(x) + I(-x) + 2\mathcal{R}\left\{e^{i\phi}\langle \mathbf{E}(x)\mathbf{E}^*(-x)\right\}\right]. \end{aligned} \tag{2.19}$$

By applying Eqn. 2.15 and then Eqn. 2.16 this may be rewritten as

$$\begin{aligned} I_a &= I(x) + I(-x) + 2\sqrt{I(x)I(-x)}\mathcal{R}\left\{e^{i\phi}\gamma(x,-x)\right\} \\ &= I(x) + I(-x) + 2\sqrt{I(x)I(-x)}\,|\gamma(x,-x)|\cos\left(\langle\omega\rangle - \phi\right). \end{aligned} \tag{2.20}$$

By closing the path to each mirror it is possible to measure $I(x)$, $I(-x)$, and thereby find the spatial coherence of the field for any point along the detector. The interferometer may be improved upon in several ways. Using a system of standard mirrors creates a more robust design as it eliminates the crux of the rooftop mirror and may also be used to flip the field about either or even both axes [34, 35]. Here the field geometry may of course be generalized as $\mathbf{E}(\mathbf{r})$ where $\mathbf{r}(x, y)$. Moreover, upgrading the setup to a scanning WFI is possible by making the path length (Δz) adjustable which allows for the measurement of temporal coherence as well.

There are many methods for automatically conducting fringe analysis using computation. Not only are these methods often faster and less work-intensive, but they have also been shown to accurately produce phase maps without the necessity of finding fringe centers or assigning a fringe order [36]. A common method and the one used here is the Fourier transform method, which has demonstrated a high level of tolerance for system-independent noise [37]. The process for the Fourier transform method was first outlined by Takeda et al. [38]. A measurement of the dark current is collected with every set of measurements, which is then subtracted away. The intensity of the interference image is then normalized by

$$I_{\text{norm}} = \frac{I_{\text{int}}(x, y) - I_1(x, y) - I_2(x, y)}{2\sqrt{I_1(x, y) I_2(x, y)}}, \tag{2.21}$$

where I_1, I_2 are the single-arm measurements and are interchangeable. A two-dimensional Fourier transform is then taken which reveals three peaks. A main center peak is flanked by two smaller peaks, and either of the smaller peaks may be selected as the new center for the data, and the others are removed. The inverse Fourier transform is then taken which gives the complex degree of coherence ($\gamma(x, y)$). Regardless of the method selected the collected data will be limited by the alignment of the fields meaning that careful tuning of the WFI's and positioning of the arrays is crucial.

2.2.2 Beam Shape and Polarization

Neither the geometry of the field emanating from a laser nor its polarization have been listed in the key properties of a laser, yet these properties are often important. There are generally two methods for describing the shape, or mode, of the laser beam. These are in terms of the Hermite-Gaussian (HG), or Laguerre-Gaussian

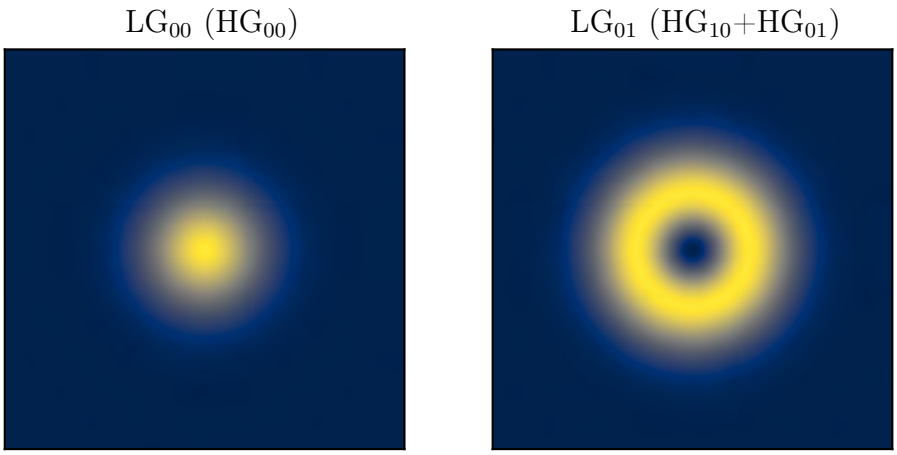

Figure 2.3: Examples of the modes exhibited in the k-space.

(LG) mode. In that any possible mode may be described by a superposition of HG or LG modes, both HG and LG modes represent a complete set of solutions to the paraxial Helmholtz equation in the Cartesian and cylindrical coordinate systems, respectively. To push this point even further, it was shown that both LG and HG modes may be generalized to the elliptic-cylindrical coordinate system in what are referred to as Ince-Gaussian (IG) modes [39]. There are two fields relating to the k-space of the plasmonic nanolaser investigated here which are important to this thesis. One is a sort of Airy disc which may be approximated to the LG$_{00}$ mode [40] and the other resembles the LG$_{01}$ mode. These are shown in Fig. 2.3, and will typically be referred to as the bright and dark modes, respectively. The primary point of this is to say that choosing to refer to the modes of this, or any other laser in terms of its HG, LG, or IG mode does not constrict the laser to some regime. The other purpose is it starts to illustrate that the toroidal LG$_{01}$ mode may be considered a composite of fields that together give the field shown in Fig. 2.3. In fact, the LG$_{01}$ mode is simply the sum of the HG$_{10}$ and HG$_{01}$ modes [41, 42].

Much of this work surrounds the dark mode, more discussion of the nature of the polarization in the dark mode appears later, but the LG$_{00}$ bright mode is also prominent in many of the measurements. Lasers are usually designed to operate in the Gaussian (0,0) mode, as it has a smaller beam diameter than other possible modes, and may therefore be focused to a smaller spot size. It is also common for this beam to be linearly polarized [28]. Linearly polarized light is simply a special

case of elliptical polarization. In fact, any light wave may be taken to be some form of elliptical polarization as it is simply a generalization of the wave equations [33].

$$\left.\begin{aligned} E_x &= a_1 \cos(\tau + \delta_1) \\ E_y &= a_2 \cos(\tau + \delta_2) \end{aligned}\right\} \Rightarrow \begin{cases} E_\xi = a \cos(\tau + \delta_0) \\ E_\eta = \pm b \sin(\tau + \delta_0) \end{cases} \tag{2.22}$$

Where τ represents the variable part of the phase factor, δ is the phase angle, and a and b are amplitudes. This is referred to as elliptical polarization because the path that the polarization vector of the wave traces out as the wave moves along E_z. Whether the components of the vector are taken to be E_x, E_y or the generalized E_ξ, E_η, they will oscillate 90° out of phase tracing out sine waves in their respective plane. The sum intensity of these sine waves will be seen in the intensity of the field when it is viewed behind an analyzing linear polarizer and rotating it through 360°. These are the concepts illustrated in Fig. 2.4

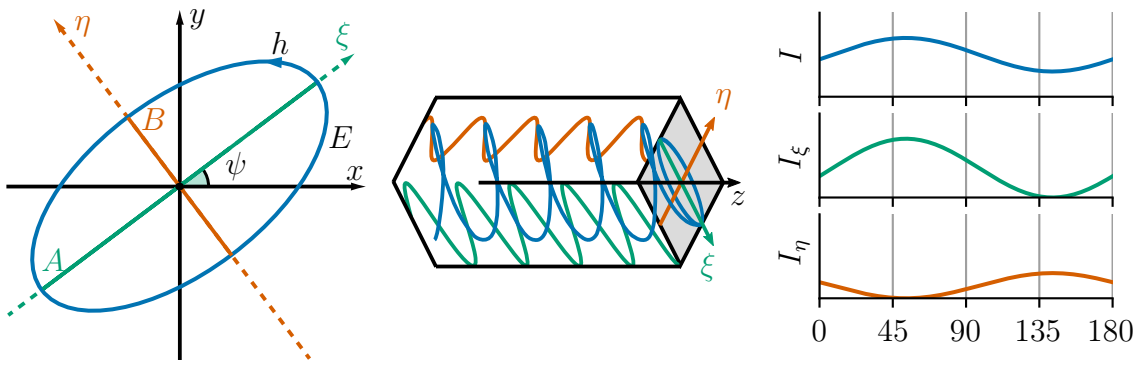

(a) (b) (c)

Figure 2.4: Evolution of elliptically polarized light. (a) The geometry of the polarization ellipse. (b) How the components of a traveling elliptical wave trace out sine waves that are 90° out of phase. (c) Summation of the intensities of the two components.

In 1852 G.G. Stoke defined four correlated parameters for the characterization of an elliptical wave. Adding a variable χ as the hypotenuse of A and B in Fig. 2.4a which relates the ellipticity. In this form, the so-called Stokes parameters are given

as

$$\begin{aligned} S_0^2 &= S_1^2 + S_2^2 + S_3^2 \\ S_1 &= S_0 \cos(2\chi) \cos(2\psi) \\ S_2 &= S_0 \cos(2\chi) \sin(2\psi) \\ S_3 &= S_0 \sin(2\chi). \end{aligned} \tag{2.23}$$

S_0 is proportional to the full intensity of the wave. The remaining relate to the orthogonal components of the wave. S_1 relates to 0° versus 90°, S_2 relates to 45° versus 135°, and S_3 relates to left versus right circular polarization in the wave (shown as h in Fig. 2.4a). The values of S_1 and S_2 for a given field may be found using a linear polarizer. S_3 requires measurements with a half-wave plate. Combined, these may be used to quantify how polarized or unpolarized a field is, as the degree of polarization with

$$\text{DOP} = \frac{I_{\text{pol}}}{I_{\text{total}}} = \frac{\sqrt{S_1^2 + S_2^2 + S_3^2}}{S_0^2}. \tag{2.24}$$

Since the last three Stokes parameters all have the first parameter in them, this value may be considered to be the Euclidean distance of the three values (which is indeed the case if they are considered to be points in the Poincaré sphere) normalized by the total intensity of the field [28, 33]. Degree of polarization is a valuable tool for quantifying the polarization of a field as it characterizes the orthogonal components of the field allowing for a full description of its polarization [43]. Without knowing anything about the state of the circular polarization it is not possible to find the DOP, but it is still possible to quantify the linear polarization. There does seem to be some ambiguity for finding the degree of linear polarization (DOLP) [44], but one common method for calculating it is to simply ignore the circular component when calculating DOP [44–46]. In terms of the Stokes parameters, this gives

$$\text{DOLP} = \frac{\sqrt{S_1^2 + S_2^2}}{S_0^2}. \tag{2.25}$$

Applying some geometry to Fig. 2.4a the necessary Stokes parameters may be expressed as

$$\begin{aligned} S_0 &= A^2 + B^2 \\ S_1 &= (A^2 - B^2) \cos 2\psi \\ S_2 &= (A^2 - B^2) \sin 2\psi. \end{aligned} \tag{2.26}$$

Where A is the major axis of the ellipse and may be taken as the peak intensity of the wave, B is the minor axis of the ellipse and the minimum amplitude of the wave, and ψ is the angle of the major axis to the measurement axis which may be taken as the polarization angle at which the peak amplitude appears. Substituting these into Eqn. 2.25 yields

$$\text{DOLP} = \frac{\sqrt{((A^2 - B^2)\cos 2\psi)^2 + ((A^2 - B^2)\sin 2\psi)^2}}{A^2 + B^2} = \frac{(A^2 - B^2)\,|\sin 4\psi|}{2(A^2 + B^2)} \quad (2.27)$$

The DOLP then quantifies how linearly polarized the field is on a 0-1 scale (1 being fully linearly polarized) and may be found by rotating a linear analyzer through the field to establish the geometry of the polarization ellipse.

2.3 The Plasmonic Nanolaser

In Ch. 1 it was stated that a multitude of constructions for plasmonic nanolasers exist. While many share a theoretical framework with the one used for this thesis, only the concepts related to this nanolaser will be explored. As previously mentioned, there are three key components common to any laser. Namely, the gain medium, cavity, and pump, which should first be identified in the present system. The pumping in this case comes from a femtosecond laser. Femtosecond lasers are a class of lasers that take advantage of the phenomenon of mode-locking to produce ultra-short, high-energy pulse trains. Mode-locking is not a central concept here but may be understood simply as a group of techniques for generating light pulses that have a duration approximately equal to the inverse of the linewidth [31]. The purpose of this pumping is clearly to excite some gain medium. In this system, the gain medium is a laser dye. Laser dyes are typically organic molecules which are noted for their fluorescence as well as their wide absorption and emission bands. As is usually the case in fluorescence, the dye will absorb photons from the pump beam, and there will be an emission which has been Stokes-shifted to higher wavelengths. These features are directly related to the structure of the dye molecule. For many dye molecules, the electrons within the molecule are free to move across the middle of the molecule but are pushed away from the edges by repulsive methyl groups (a carbon bonded to three hydrogen) at the ends [31]. It is common for the dye to be suspended in water or an organic solution, as is the case here [28]. The relaxation time for the dye molecules is slow compared to the pump laser, which ensures the

desired population inversion such that the cascade of stimulated emission occurs. Now that there are some photons moving through the system, they will stimulate the emission of photons from other excited dye molecules, and so on, as described in Sec. 2.2. From here, the plasmonic nanolaser begins to differentiate itself. The gain dye is surrounding a periodic lattice of metal nanoparticles. A more generalized way to view the mirrored cavity of a conventional laser is to say that the mirrors simply establish the boundary conditions which dictate which wavelengths can survive in the cavity. Rather than mirrors, the boundary conditions are established by these nanoparticles which have been fabricated on to the glass substrate. As demonstrated in Fig. 2.5 in the case of mirrors, it is necessary that the wave nodes are at the mirrors, here it is necessary that either the nodes or antinodes are at the particles. If the boundary conditions are not met, the wavelength will become extinct. If they are met, then that associated wavelength is enhanced. This feature

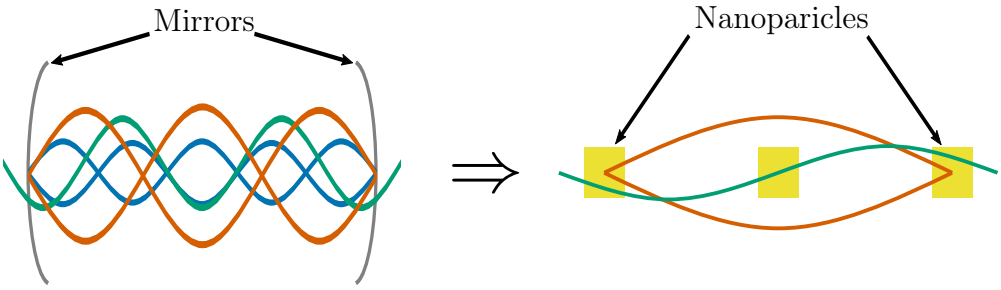

Figure 2.5: Relation of boundary conditions in a conventional laser to the nanolaser.

then sets up the limitation of what wavelengths may be emitted as they are a direct result of the periodicity of the array, and related to the refractive index (n) of the substrate as

$$\lambda = n \cdot p. \tag{2.28}$$

The emission is further enhanced by resonances in the particles called localized surface plasmons resonances (LSPRs), which arise from the pump beam's interaction with particles in the lattice and the substrate thus increasing the lasing [47]. The nature of surface plasmons will be discussed further in Sec. 2.3.1.

The LSPRs hybridize with diffraction orders which occur because of the periodic lattice and generate surface lattice resonances (SLRs), [5]. These resonances have been shown to take on two different modes. The constitution of these modes is

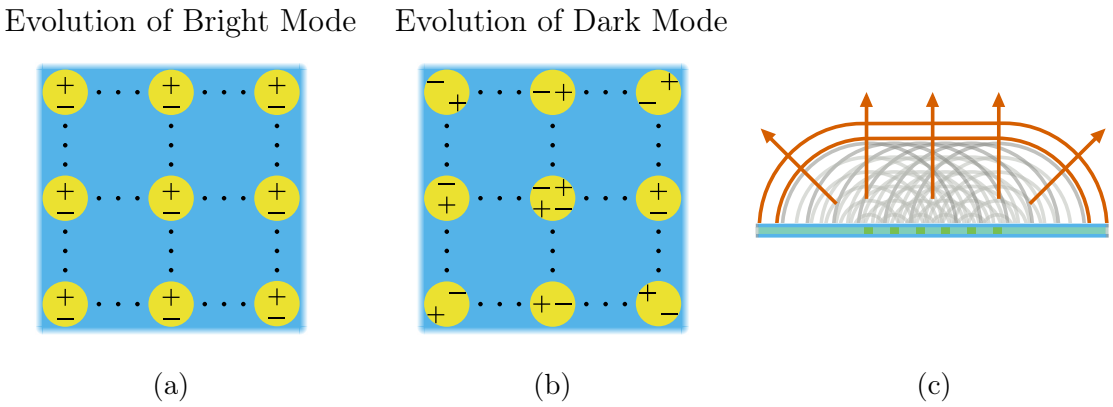

Figure 2.6: Illustration of how the particles generate the two observed modes. In (a) the particles are polarized and will mainly radiate from the center of the lattice, where as in (b) counter-propagating waves have induced a subradiant quadrupol. In (c) the Huygens-Fresnel principle is demonstrated.

illustrated in Fig. 2.6. In one case, the particles are polarized across one axis and therefore radiate along the other. This is the bright mode of Fig. 2.6a and while the amplitude at the edge will inevitably decrease, in the center of the array, the constructive interference from counter-propagating waves creates a constant phase. Conversely in Fig. 2.6b the counter-propagating waves have caused destructive interference at each particle location generating a standing wave. Particles at the nodes of this standing wave have quadrupolar charge distribution generating the dark mode, as the particles at the antinodes are still dipoles, this technically makes this a hybrid mode. With the particles of the lattice now behaving as nodes and antinodes, they will become point sources emitting spherical waves that together form the beam as in the Huygens-Fresnel principle illustrated in Fig. 2.6c. The bright and dark modes which will appear in the far field as resembling the LG_{00} and LG_{01} modes, respectively, as described earlier.

2.3.1 Surface Plasmon Polaritons

The generation of plasmons when the pump beam is incident with the metal-glass interface is crucial to the generation of lasing in plasmonic nanolasers. The gold and glass belong to two different classes of material referred to as double-positive (DPS) and single-negative (SNG), respectively. These classes are divided based on whether

the permittivity (ϵ) or permeability (μ) are both positive, or if one is negative (a third and unrelated class of material sees both negative). These characteristics relate closely to their appearance. At visible wavelengths, glass and other dielectrics are transparent, while gold and silver with their negative permittivity are reflective. When these two materials are joined, interesting optical phenomena are able to occur at the boundary. To start, it is practical to consider total internal reflection where at specific angles a beam of light is perfectly reflected from the junction of two dielectrics (two DPSs), however, the field actually penetrates beyond the interface by a small amount as it is being reflected with what is called an evanescent wave. In the case of the dielectric-metal junction, there is a reflection for any angle and thus the generation of an evanescent wave is not angle-dependent, but at certain angles, it is now possible to generate a surface wave in the metal [28]. In describing the mechanics of plasmons Heinz Raether first approximated the metal as a dense liquid of free electrons or a plasma, thus a single quantum of oscillation in the plasma is a plasmon [48]. Fig. 2.7 illustrates the surface plasmon propagation. The

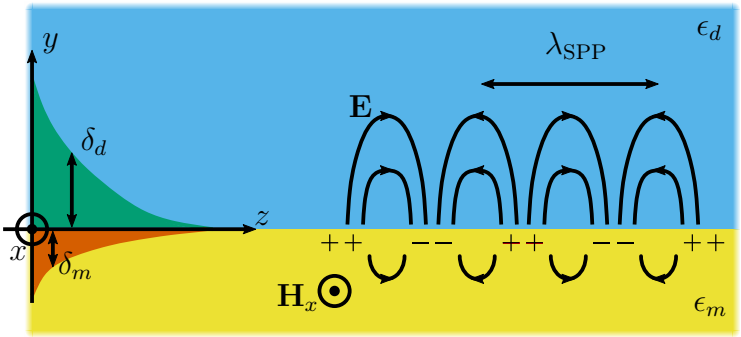

Figure 2.7: Electric and magnetic fields of a propagating surface plasmon.

penetration of the electric field into the metal (m) and dielectric (d) is illustrated (δ) and clearly decays exponentially in the z direction and does not penetrate as deeply into the metal side of the interface. The magnetic field ($\mathbf{H}$) is oscillating in and out of the page [32]. The change in sign of permittivity at the boundary forces a change in the sign of the electric field which then results in the generation of an optical wave. The coupled optical wave and surface plasmon are called surface plasmon polaritons (SPPs) [28], and when this field becomes radiative, a powerful light emission occurs [48]. This can be taken a step further when metal particles with

sub-wavelength dimensions and smooth surfaces on a dielectric are considered. Here, the surface geometry means that it is no longer a unique critical angle for the light interaction, and the size causes a shift in the charge for the whole particle generating the localized surface plasmon polariton (LSP) if the resonance frequency of the lattice structure is matched by the excitation frequency, the LSPR is realized [28].

2.3.2 Bound States in Continuum

A result of the periodic lattices in the plasmonic nanolaser is the appearance of bound states in continuum (BICs). Shortly after the emergence of quantum theory, evaluation of Schrödingers equation suggested the possibility that bound states could exist above the continuum threshold, but it was not until many years later that it was found that this held true for many wave phenomena [49, 50]. BICs are coexistent with unbounded/continuum states but are spatially bounded [50]. Very recently, lasing from BICs has been demonstrated [49] and therefore identifying the BICs in the arrays is a further way to characterize the lasing capabilities of the arrays. It has been shown that careful variation of the particle periodicity and diameter allows for all four fundamental BICs to be produced by the same system. In the far field, the BICs will appear as a cylindrical vector beam and identification of the BICs is possible by examining the polarization [24]. This means that any of the four BICs may be present in any of the arrays considered in this thesis. However, by comparing which parts of the far field is visible after it has passed through the analyzer to those illustrated in Fig. 2.8 it will be possible to know which of the BICs exist. The polarization angles here, and for the remainder of this thesis, are considered from the vertical y-axis, anticlockwise. For example, if the analyzer is set to 90° and the observed field is coming from a known dark mode, and there is illumination on the horizontal axis, it is evident that the BIC type is TM. In addition, if the analyzer is set to 135°, and the illumination is in the top right and bottom left, it is indicative that the topological charge is +1. If these are from the same initial beam, it shows that the fundamental BIC is TM+1.

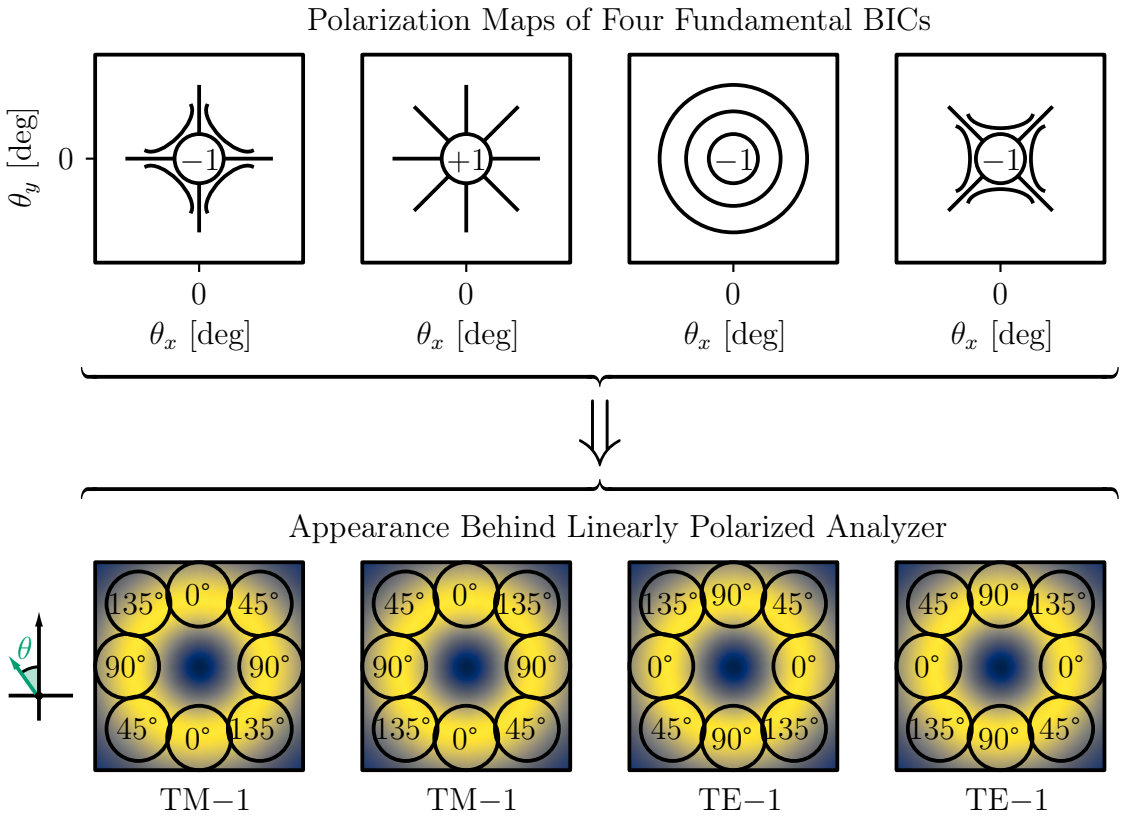

Figure 2.8: Polarization maps of the four fundamental BICs and the angle of polarization in each region.

Chapter III

Experimental Setup & Methods for Data Collection

The purpose of the setup is to excite the dye molecules and arrays on the sample slide but to do so in a way that only one array is excited at a time, and then to simultaneously capture three different images of the resulting emission. This chapter focuses on describing the setup used to collect the data for this thesis.

3.1 The Setup

Fig. 3.1 provides a representative model of the experimental setup and its key components. The pump beam is produced by the Quantronix Integra-C 3.5 which emits a train of 130 fs pulses at 1 kHz. Each pulse carries a maximum of 3.5 mJ in the form of vertically polarized 800 ± 10 nm laser light [51]. The beam is split onto other experiments before arriving at the setup. Following the path of the beam through the setup, it first passes through a half-wave plate mounted in a motorized rotation stage followed by a horizontal polarizer. Using a digital power meter, the half-wave plate is rotated such that the pulse energy is attenuated to 2 µJ. A custom Arduino-controlled aluminum shutter prevents the beam from entering the system and possibly damaging components when it is not in use. An iris diaphragm helps block undesired light before it is focused via a mirror onto the sample slide. On the way to the slide, the beam passes through a quarter-wave plate circularly polarizing the light.

The sample slide is held in place by a custom 3D printed mount which is fitted to a three-axis (xyz) stage. The pump beam creates the excitation of the dye and

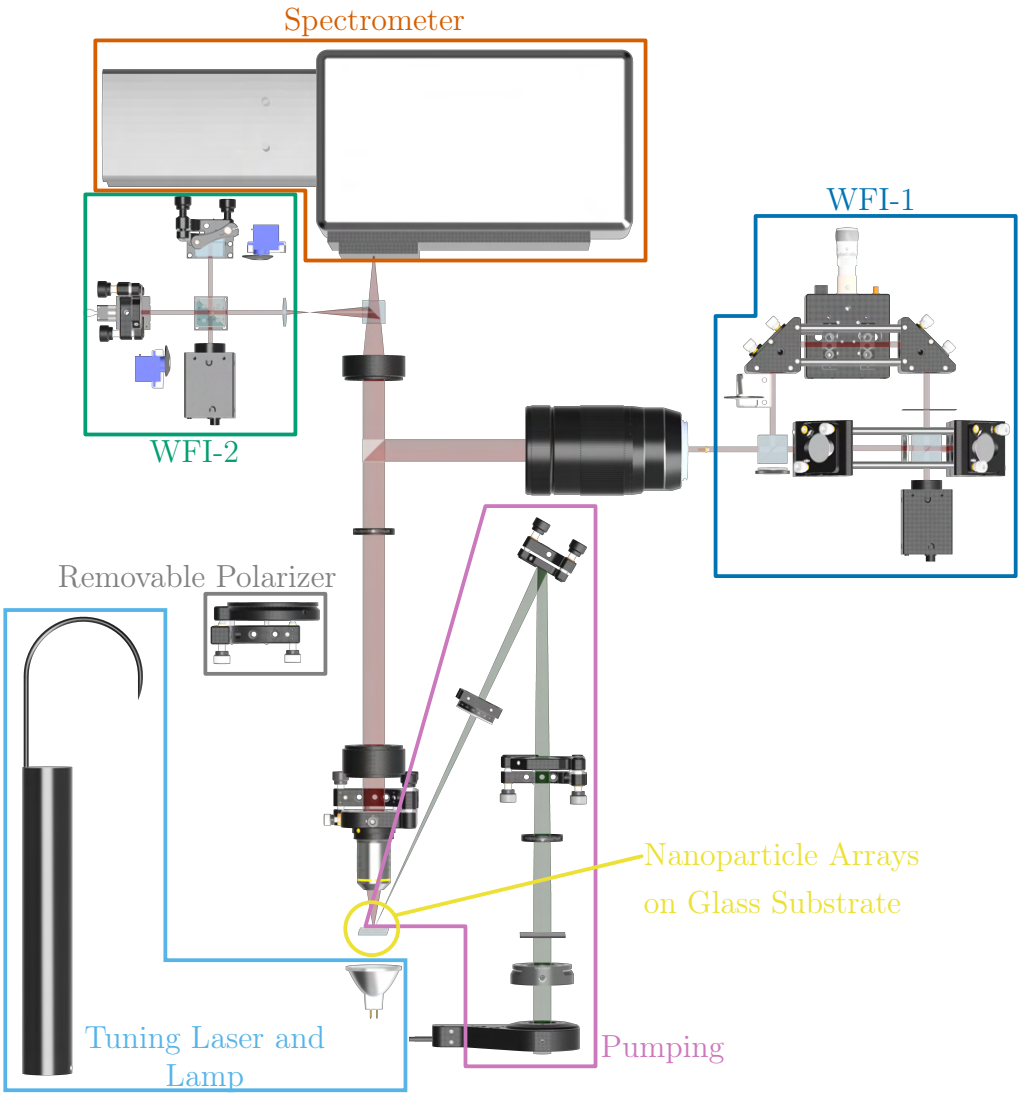

Figure 3.1: Model of the experimental setup. The key components include the pumping beam and sample with arrays. The emission is then collimated and directed towards the three measuring devices (Real-Space WFI , k-space WFI, and Spectrometer). The polarization of the emitted beam may be adjusted using the removable polarizer. A separate laser and lamp are used for aligning the elements of the experimental setup.

which is of course enhanced by the nanoparticles to induce lasing. This results in a beam that is then collimated by first passing through a 10X microscope objective, and then a lens with an effective focal length of 200 mm. A linear polarizer mounted in a manually rotating stage could be added or removed from the system at this point to polarize the field to some desired angle. Another iris diaphragm is used to block higher-order emissions from propagating further. If necessary, various neutral density filters could be added here to both protect the imaging optics and prevent saturation. A 30:70 beamsplitter directs 30 % of the field towards a camera objective which is then focused into the first wavefront folding interferometer and camera. The 70 % of the beam that is transmitted is incident on a 100 mm lens acting as a Fourier lens before passing through a 50:50 beamsplitter. With half of the field passing to the spectrometer, and half towards the second WFI. The Fourier lens allows for imaging of the k-space as described in Sec. 2.1. Finally, the setup also features a halogen lamp and helium-neon laser, both of which helped tune and align the system.

The resulting field in each of the interferometers is captured by FLIR Grasshopper 3 GS3-U3-32S4M-C cameras which utilize a 2048×1536 pixel CMOS sensor with a global shutter allowing for the simultaneous capture of each of the $3.45\,\mu m \times 3.45\,\mu m$ pixels [52]. The other terminus for the plasmonic nanolaser beam is the Andor Kymera 193i spectrometer. The spectrometer was setup to use the 1200 line per mm grating, allowed for measuring the spectrum in approximately 0.21 nm increments [53]. This spectrum was recorded by the attached Newton EMCCD DU970P detector from the same manufacturer. The cooled electron multiplying CCD allows for capturing a maximum of 649 spectra per second on a 1600×200 array of $16\,\mu m \times 16\,\mu m$ pixels, giving a two-dimensional image of the spectrum with one axis for position and the other for the wavelength [54]. A MATLAB script allowed for simultaneous collection of data from all three sensors. There are two aspects of the setup which require more detailed considerations.

3.1.1 The Arrays

The gold nanoparticle arrays were patterned onto a glass slide (borosilicate, $n_{800} \approx 1.52$) using electron beam lithography, and evaporative metal deposition to create a nominal particle height of 56 nm. As mentioned in Sec. 2.3 the gain medium for this type of plasmonic nanolaser is a fluorescent dye. In this case, IR 792 is used, and it

is diluted with index matching fluid (matching the borosilicate glass slide substrate). From Fig. 3.2b it is clear that IR 792 follows the general structure of other laser dyes presented in 2.3with the methyl groups at either end of the molecule separated mostly by carbon. The dye mixture is then covered by a glass slide cover. Particle periodicity and diameter within each array are constant but are varied incrementally across the slide to give a variety of geometries for measurement. A model of the slide with arrays is given in Fig. 3.2a. The diameters vary from 80 nm to 220 nm in 10 nm increments, and periodicities 570 nm, 580 nm, and 590 nm. Nine sets of arrays were patterned onto the sample.

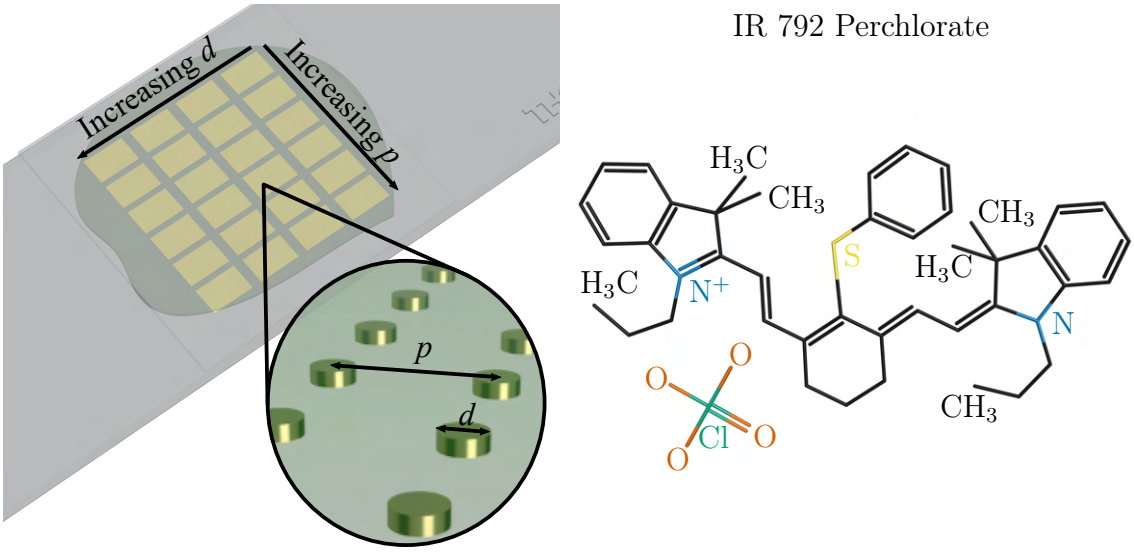

(a) (b)

Figure 3.2: Details of the nanoparticle arrays and dye. In (a) the general geometry of the patterned arrays with IR 792 on the borosilicate substrate. The molecular structure of IR 792 dye is shown in (b) [55].

3.1.2 The Wavefront Folding Interferometer

The two wavefront folding interferometers are crucial in collecting coherence data from the system. The first collects real-space coherence data and the second is for the k-space measurement, each may be viewed in Figs. 3.3a and 3.3b respectively. For compactness, these will mostly be referred to as WFI-1 and WFI-2 from this point. Each WFI features shutters driven by Arduino-controlled servos and activated by

MATLAB script. These operate sequentially to allow the camera to first measure part of the field with one arm open then the field with the other arm open, with both arms open, the interference is measured, and finally, both arms close such that the dark current may be measured. There are two key differences in the WFIs. First, it can be seen from the models that WFI-1 uses a system of flat mirrors, whereas WFI-2 relies on a single rooftop mirror. Using the mirrors creates a more robust system and eliminates the dead zone that exists in the crevice of the rooftop mirror [35]. The other difference is that WFI-1 is able to flip the field about both axes (horizontal and vertical), where as WFI-2 follows the more traditional design as described in Sec. 2.2.1 and uses the rooftop mirror to flip the field about the horizontal axis. As the scanning of the interferometer arms was not used, it is of only minor interest that the path length in WFI-1 is controlled via a micrometer stage, and WFI-2 has a Thorlabs motorized translation stage which is again activated via MATLAB and is described by the manufacturer to be accurate to 0.05 µm.

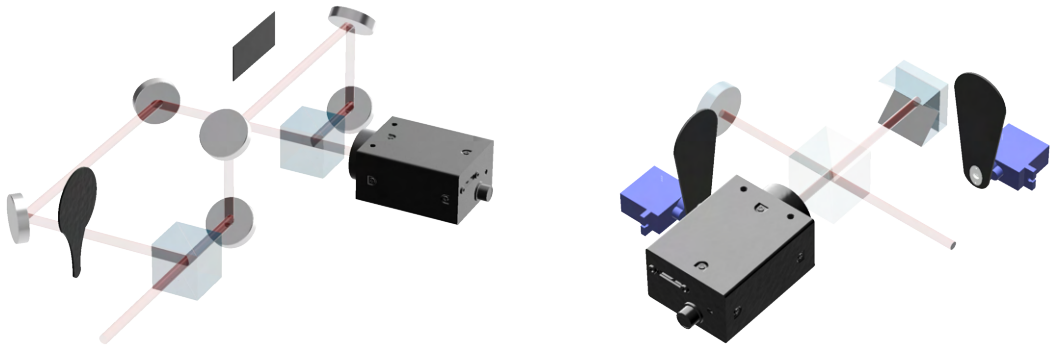

(a) (b)

Figure 3.3: Models of the two WFIs used for measuring the coherence of the emitted field. Real-space measurements were captured by WFI-1 (a), and WFI-2 (b) is positioned after the Fourier lens to capture k-space measurements.

3.1.3 Tuning the Setup

Two elements included in the setup aid in tuning the experimental setup. One is a HeNe laser. A system of mirrors (not shown) reflects the beam into the system. With the slide removed, the beam passes through the setup, and using targets, it is possible to verify that the various mirrors, beamsplitters, and lenses are properly aligned. The HeNe laser is also used to align the slide when installing it by ensuring that the beam is reflected back down its path of incidence. The second tool is the halogen lamp which sits directly behind the slide stand. Taking advantage of the very small coherence length of the lamp ($L_c \approx 16\,\mu m$ [56], though fringes from the lamp were only visible for a single 0.05 µm step of the translation stage), it is then possible to establish with a high degree of certainty where the path length difference in the arms is approximately zero. Finally, the halogen lamp is also used to illuminate the slide such that the correct array could be found, centered on the cameras, and tested.

3.2 Measurements

The overreaching target of the data collection was to measure the polarization of the beam for a variety of particle diameters. To achieve this, the linear polarizer was removed to first record the unpolarized beam. Then, the polarizer was replaced and starting at 0° measurements were made in 45° increments up to 135°, in affect providing measurements for all 360° of polarization. The particle diameters from 160 nm to 220 nm were taken as a representative sample. One challenge that has yet to be addressed is that the IR 792 and index matching solution damages the arrays over time, and of course, there is always the possibility of difficulties in fabrication, etc. The result of this is that not all measurements were collected using the same periodicity. A particle periodicity of 570 nm was used as the default, however in a few cases the use of the 580 nm or 590 nm arrays was needed. This change is indicated where necessary. The direct processing of each data set is more or less unique to the type of data collected and is discussed in detail along with the presentation of the data in the next chapter.

Chapter IV

Data Processing & Analysis

In this chapter all of the collected data from each measurement will be presented, and then analyzed. Each measurement was first corrected to account for the filter according to

$$\frac{I}{I_0} = 10^{-D} \Rightarrow I_0 = I \cdot 10^{D},$$

where I is the measured intensity, D is the filter density, I and I_0 represent the field intensity without filtering, respectively. Then the features were scaled for each set of measurements for each array such that they could be visualized on the same scale. The intensity units for all three sensors are arbitrary and are therefore not given.

4.1 Spectral Measurements

As described in Sec. 3.1 the spectrometer was able to record both the spectral distribution of the field and the y-position. The slit opening for the spectrometer has been set wide to prevent problems that may arise from a narrow slit with the analyzer set to 0°. This had the added effect that the spectrometer images would also show the shape of the field. For this reason, a script was written in Python to help identify the central wavelengths for each mode. In all of the following figures, the dark mode is highlighted in green, and when visible, the bright mode is highlighted in orange. In all measurements, the data has been cropped to display a region of 40×40 pixels for an image that is 640 µm tall with a wavelength range of 40 nm.

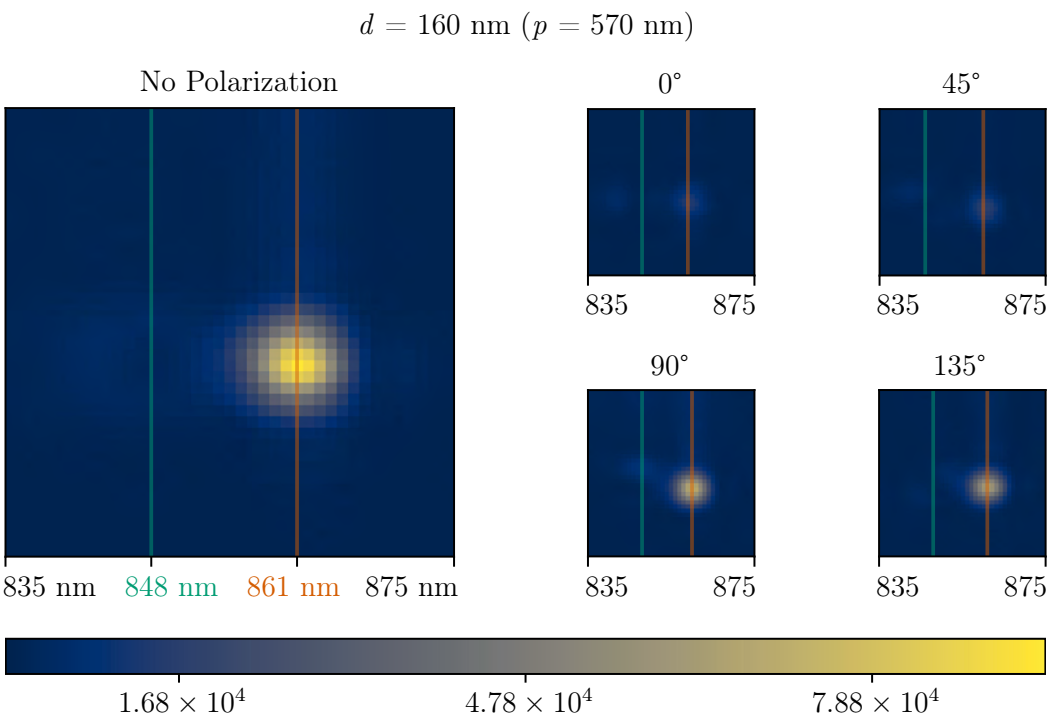

Figure 4.1: Spectral k-space measurements of the $d = 160\,\text{nm}$ array.

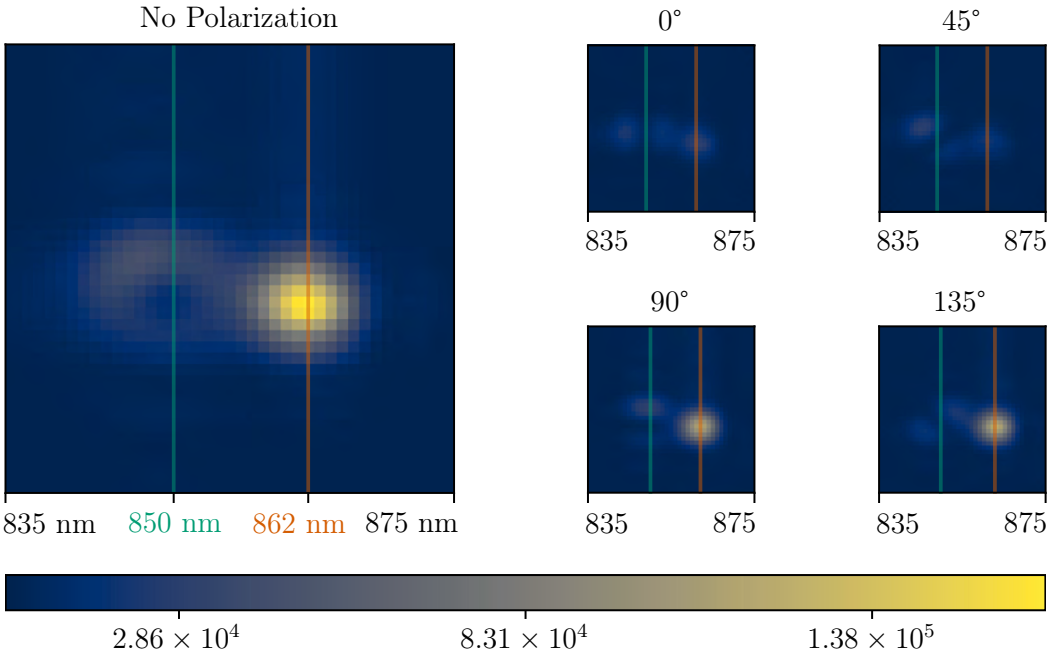

Figure 4.2: Spectral k-space measurements of the $d = 170\,\text{nm}$ array.

4.1.1 $d = 160\,\mathrm{nm}$

In Fig. 4.1 the bright mode is distinct at about 861 nm, and a faint image of the dark mode may be observed at roughly 848 nm. With the analyzer in place, it is obvious that the field is much more intense for 90°, and 135° cases.

4.1.2 $d = 170\,\mathrm{nm}$

Fig. 4.2 shows that the dark mode is beginning to become more intense, and the peak intensity measured is higher than in the previous case. Both modes have also shifted slightly towards longer wavelengths. The polarization of the bright mode follows the same trend, while as expected, the toroid of the dark mode is missing segments depending on the polarization.

4.1.3 $d = 180\,\mathrm{nm}$

In the case of the 180 nm particles shown in Fig. 4.3, the dark mode is beginning to dominate. This is also the first case where a larger periodicity was necessary, and it is clear that there has been a larger shift towards longer wavelengths. Behind the analyzer, the bright mode has again followed the behavior like before appearing approximately as intense as the dark mode in the 90°, and 135° cases, while the dark mode intensity is generally consistent.

4.1.4 $d = 190\,\mathrm{nm}$

From Fig. 4.4 it may be seen that at a particle diameter of 190 nm the dark mode now completely dominates, and it has continued its procession to higher wavelengths. Of all the spectral measurements, this is the clear image of the toroid pattern characteristic of the dark mode, and it serves as a good example that depending on the polarization the lobes appear in different positions.

4.1.5 $d = 200\,\mathrm{nm}$

Again, the measurement of the 200 nm particle lattice has created a sharp (perhaps the sharpest) dark mode with no visible bright mode as may be seen in Fig. 4.5. The overall intensity has continued to increase, and as before, with the larger period, there has been a significant shift to larger wavelengths.

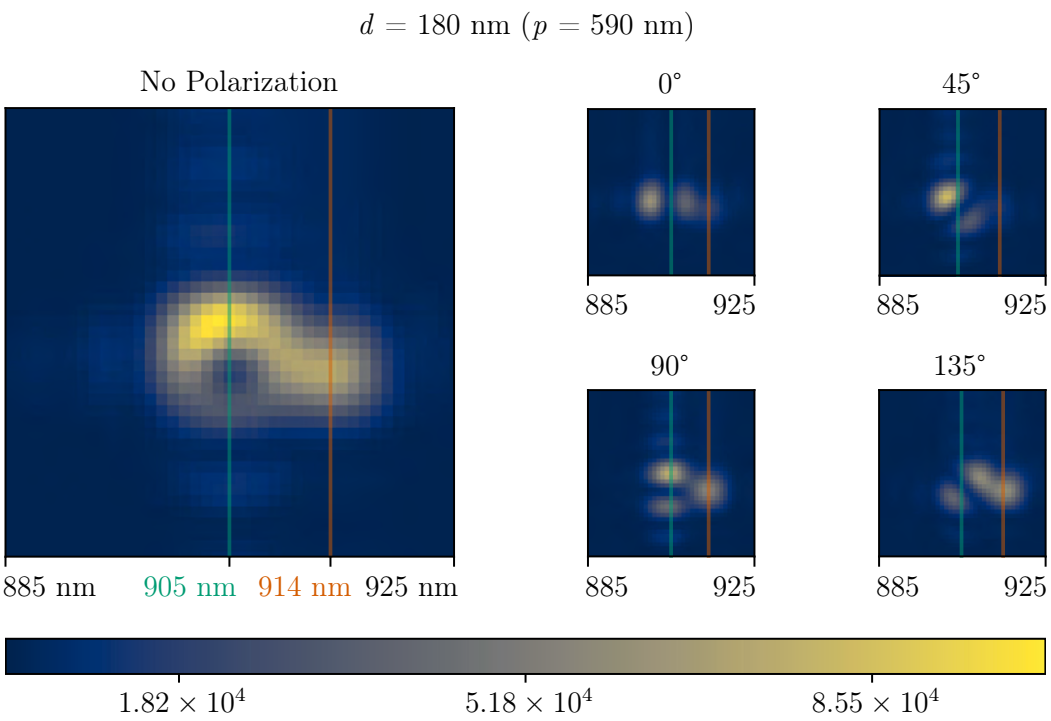

Figure 4.3: Spectral k-space measurements of the $d = 180\,\text{nm}$ array.

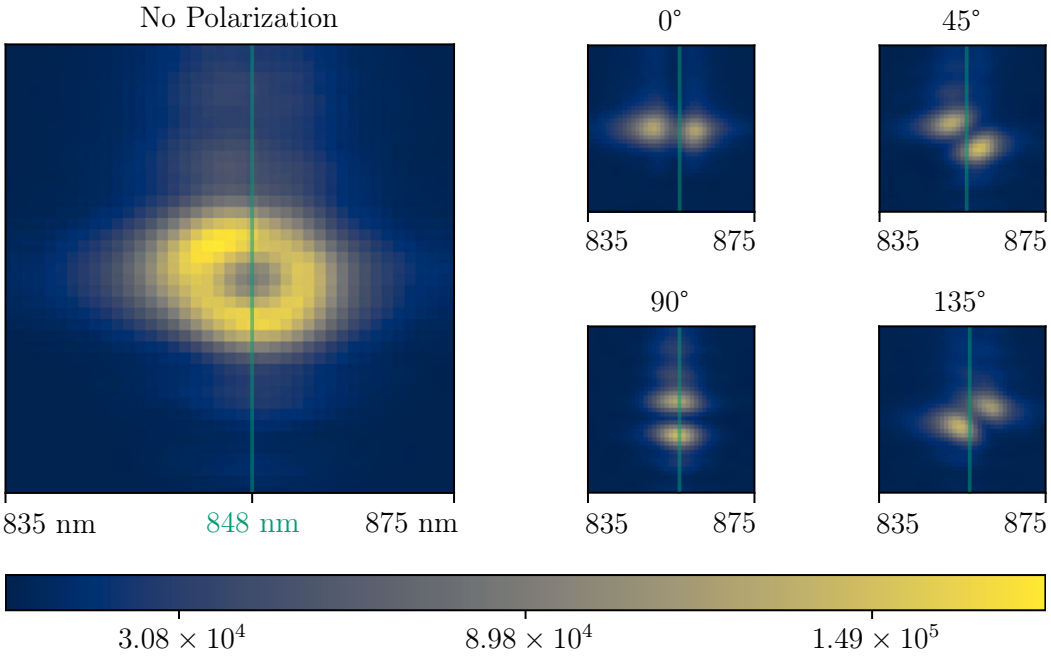

Figure 4.4: Spectral k-space measurements of the $d = 190\,\text{nm}$ array.

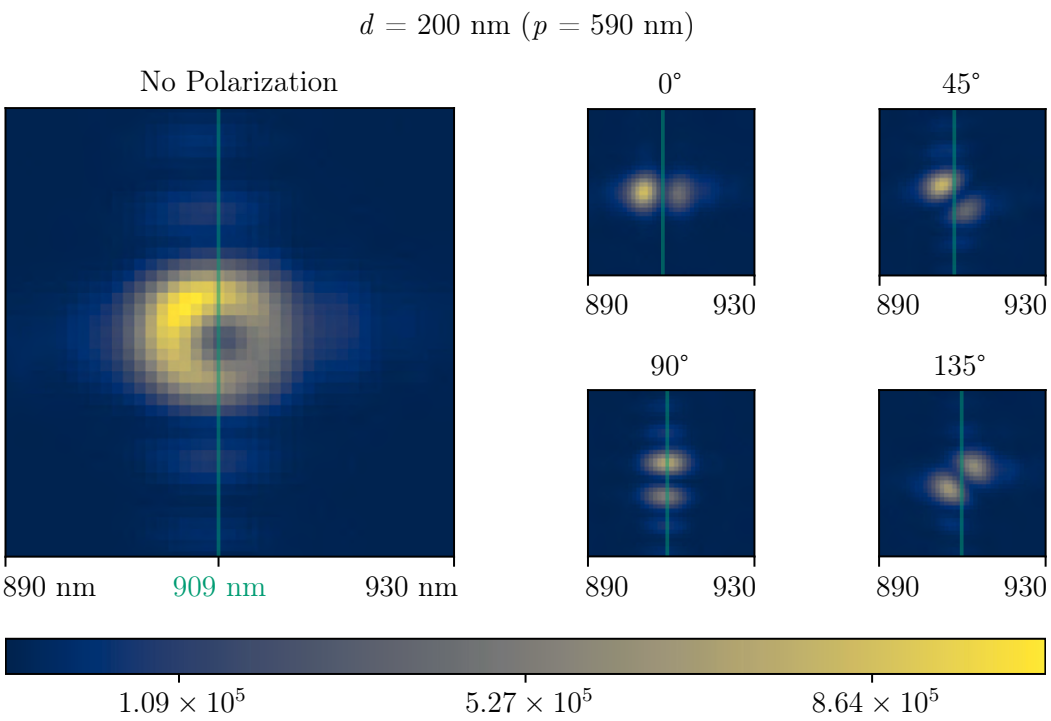

Figure 4.5: Spectral k-space measurements of the $d = 200\,\text{nm}$ array.

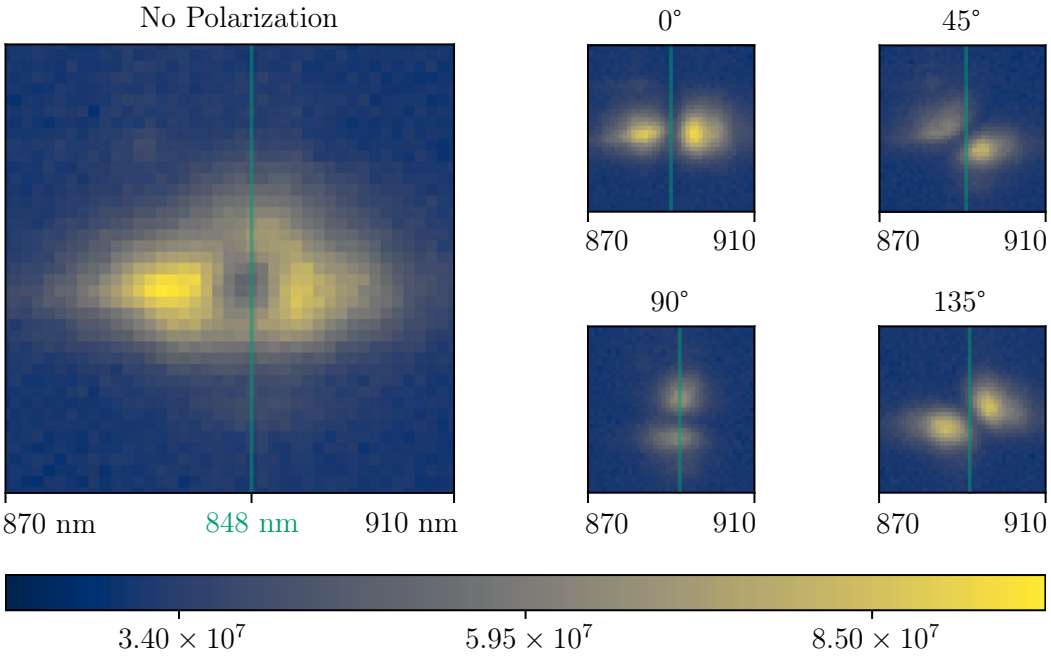

Figure 4.6: Spectral k-space measurements of the $d = 210\,\text{nm}$ array.

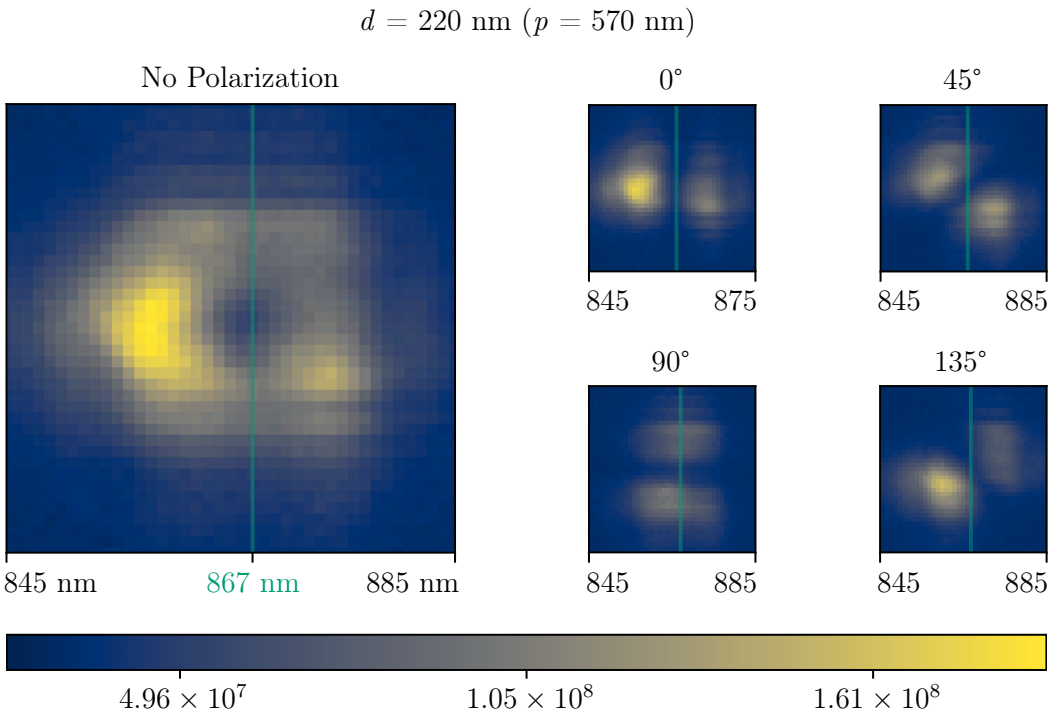

Figure 4.7: Spectral k-space measurements of the $d = 220\,\text{nm}$ array.

4.1.6 $d = 210\,\text{nm}$

Fig. 4.6 gives the only measurement of an array with a 580 nm period. The central wavelength appears somewhere between what has been seen in the other cases, but the intensity has continued to increase. Only the dark mode is visible.

4.1.7 $d = 220\,\text{nm}$

Measuring the $d = 220\,\text{nm}$ array required a combination of neutral density filters totaling a filter density $D = 5$ as the field had become so intense. The measurements given in Fig. 4.7 are once again for the lowest periodicity, and, as has been the case for particles larger than 180 nm, the bright mode is either indistinguishable or is too insignificant to register. The dark mode has continued to drift slightly towards longer wavelengths.

4.1.8 Analysis

The spectral measurements on their own provide considerable information about the output from the plasmonic nanolaser. The central wavelength of each mode is given in the respective figure, and it is evident that the greatest cause for difference is the periodicity of the array. This follows directly from the fact that the boundary conditions are established by the spacing of the particles, and hypothetically the difference of the array geometry should be able to be accounted for by considering Eqn. 2.28. In Fig. 4.8a, the refractive index for each mode has been plotted along

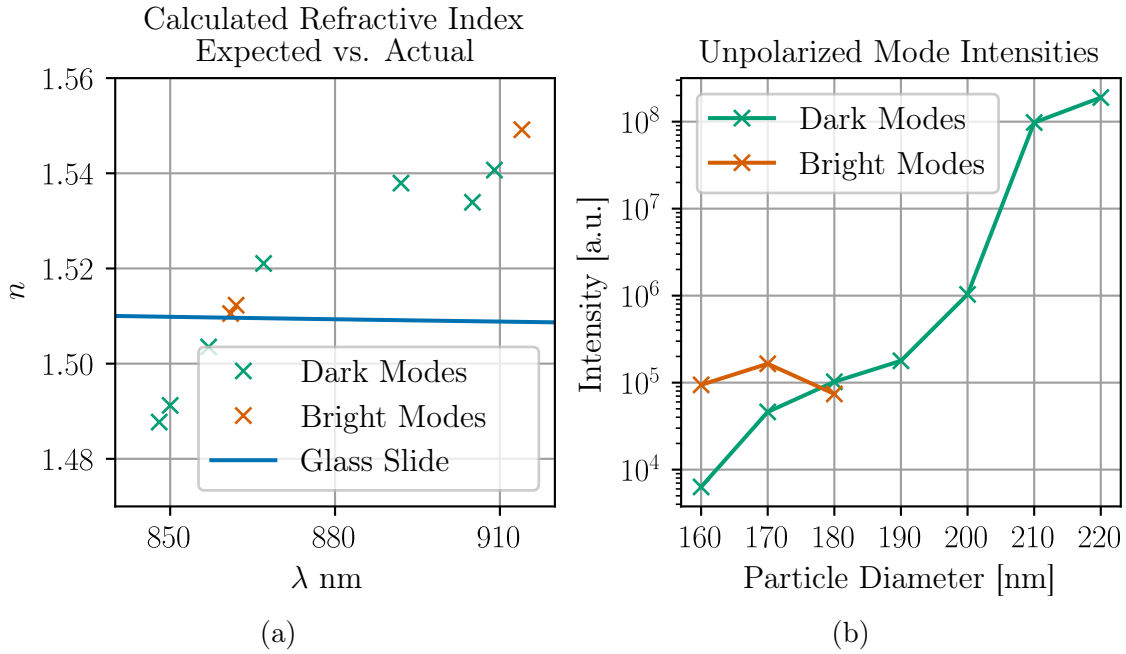

Figure 4.8: Calculated versus expected refractive indices are given in (a). The intensity of the modes without polarization is given by logarithmic scale in (b) illustrating a roughly exponential trend.

with the actual refractive index of the borosilicate glass. The values associated with the larger periodicities are grouped in the upper right corner of the plot, and the points associated with the bright modes of the 160 nm and 170 nm arrays are pretty close to ideal. There is however little other correlation. It is obvious that Eqn. 2.28 is not sufficient for explaining which wavelengths a given array geometry might produce, especially for larger particle diameters. It has been suggested that finding

the full Stokes parameters for the field might help better understand the origin of the modes and help develop a more robust model. The other important information that the spectral measurements provide is of course the intensity of each mode. The unpolarized intensities are plotted against the particle diameter in Fig. 4.8b. It is abundantly clear that the intensity of the dark mode increases with particle diameter at a roughly exponential rate. The plot also implies that there is a transition from a bright mode dominant regime to a dark mode dominant regime at around 180 nm, but more data must be collected to confirm this.

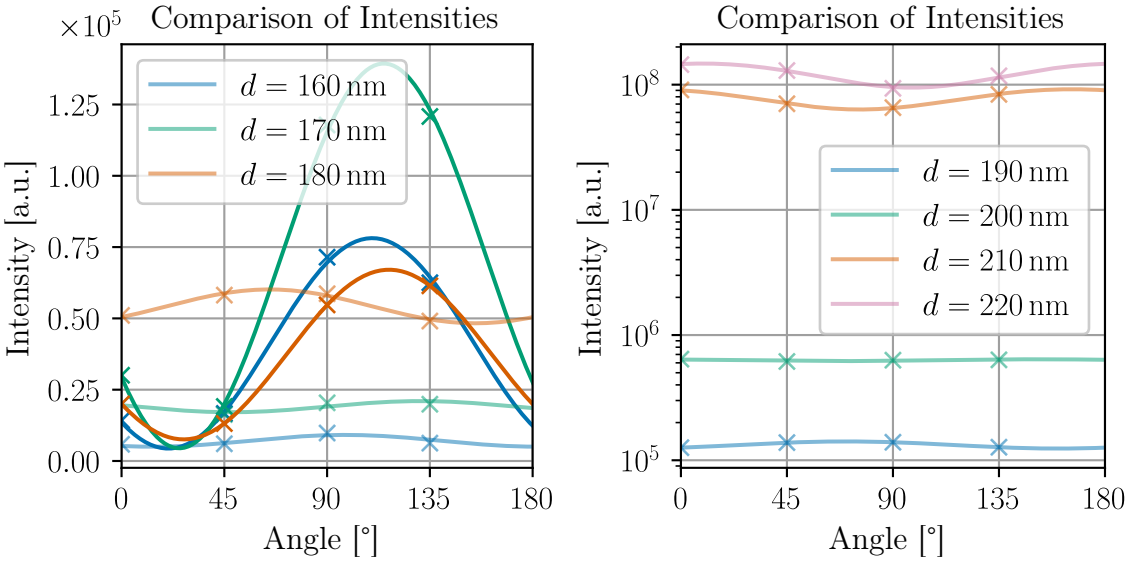

Figure 4.9: Intensity vs. Polarization angle with calculated sine fits. Lighter colors are for dark modes, brighter colors represent bright modes. Where possible (160 nm, 170 nm and 180 nm) the bright and dark modes are compared in (a), and (b) gives a logarithmic scale for the remaining arrays.

The spectral measurements are also an excellent tool for analyzing in detail the polarization of the modes. The same script which was used to identify the central wavelengths was also used to find the peak intensity of each region (i.e., the two lobes of the dark mode and the single for the bright mode). To better account for any tilting of elements in the system, etc. the two lobes of the dark mode were averaged together. Then the intensity of the polarization measurements for each mode in each lattice could then be plotted based on the angle of polarization. The result of

this is shown in Fig. 4.9. Because the 0° measurement also gives the polarization at 180° and so on, the data may easily be made to be periodic. Fitting the periodic changes in intensity to a sine wave allows for estimating the major and minor axis of the field. With that, it is possible to apply Eqn. 2.27 to find an estimation for the degree of linear polarization. This analysis is of course most relevant to the bright modes, however, the low DOLP calculated for the dark modes helps further illustrate that their intensity remains fairly constant regardless of the polarization. Table 4.1 gives the estimated DOLP as well as the major and minor axes for the sine fit of each mode.

Array	Mode	Major Axis	Minor Axis	DOLP
160 nm	Bright	108°	20.6°	0.994
	Dark	98.0°	2.20°	0.539
170 nm	Bright	114°	25.2°	0.999
	Dark	117°	48.1°	0.203
180 nm	Bright	117°	26.9°	0.974
	Dark	56.6°	47.2°	0.395
190 nm	Dark	69.9°	159°	0.131
200 nm	Dark	34.2°	129°	0.244
210 nm	Dark	175°	85.9°	0.312
220 nm	Dark	9.17°	98.0°	0.416

Table 4.1: Table of values found by sine fit.

Looking at the DOLP values in the table, it is easy to see that the three bright modes are not just highly linearly polarized but also follow a similar trend for their major and minor axes. The dark modes on the other hand exhibit a maximum DOLP of ≈ 0.539, and are wildly inconsistent, both of which should be consistent with the expectations of this type of beam. Repeating these measurements with a half-wave plate would allow for a more complete analysis of the bright mode by allowing for the calculation of the final Stokes parameter and in turn the full degree of polarization for the bright mode. An important takeaway from Fig. 4.9b is that there is a slight dip in the intensities at 90°. Assuming all the bright modes would follow a similar trend, this implies that the bright mode has truly become insignificant, and is not just being covered by the dark mode.

Array	Visible Regions				Proposed BIC
	0°	45°	90°	135°	
160 nm	··	⋱	:	⋰	TE-1
170 nm	··	⋱	:	⋰	TE-1
180 nm	··	⋱	:	⋰	TE-1
190 nm	··	⋱	:	⋰	TE-1
200 nm	··	⋱	:	⋰	TE-1
210 nm	··	⋱	:	⋰	TE-1
220 nm	··	⋱	:	⋰	TE-1

Table 4.2: Proposed BICs of the modes based on analysis of k-space measurements.

Finally, another important benefit of the wide slit providing the k-space image of the field, is that it starts to offer clues to which BICs are present in the dark modes by comparing each polarized measurement to the unpolarized case, and considering which portion of the field is still present. Either the 0° or 90° measurements are used to determine whether the BIC is TE or TM, and the 45° or 135° are then necessary to determine the topological charge (+1 vs. -1).Table 4.2 gives the results of this analysis. The illumination under polarization gives the BIC for all arrays as TE-1.

4.2 *k*-space Interferometer Measurements

Sitting behind the Fourier lens as well, WFI-2 was used to take interferometry measurements of the k-space by flipping the field vertically. This gives the spatial coherence along one axis of the k-space which is representative of the divergence of the beam in the far field. It has already been seen in Sec. 4.1 what the general shape of the field should be, but remember that here the bright and dark modes will not generate separate images, rather they will be superposed on top of each other. Each measurement has been processed using the Fourier transform method as described in Sec. 2.2.1. As the data has already been normalized in processing, and the intensity information is lost (and the units are arbitrary to begin with), the colorbars are not included. Each of the following images is 1534×1534 pixels which correlates to a $5.2923\,\text{mm} \times 5.2923\,\text{mm}$ area of interest. For consistency with the previous measurements, each image has been mirrored horizontally. This is

not necessary, but referring back to Fig. 3.1 the beam is now moving the opposite direction into the camera.

4.2.1 $d = 160\,\mathrm{nm}$

Excepting for the interference fringes, the images captured in Fig. 4.10 follow closely what was seen in the spectrometer images before. There is a clear bright mode, but the intensity of the mode under 0° and 45° polarization drops off significantly.

4.2.2 $d = 170\,\mathrm{nm}$

Fig. 4.11 again gives an expected result. Remembering that the bright mode was still more than three times brighter than the dark mode in the spectral measurements, the bright mode dominates when the polarizer is removed, but under close observation, there is a slight twisting of the fringes, which illustrates the presence of other wavelengths, and in this case, illustrate the presence of the other mode. The 0° and 45° measurements also give a faint impression of the dark mode. There is an unfortunate amount of saturation in the unpolarized image.

4.2.3 $d = 180\,\mathrm{nm}$

Looking at Fig. 4.3 and considering that in the comparable spectral measurements the dark mode was just 5 % brighter than the bright mode, it is not surprising that the LG_{01} profile has started to appear in the unpolarized image, but it is by no means dominant. An interesting pattern has started to develop in the 45° and 135° data. Rather than seeing two parts of the field as before plus another two from the flipped image (given for illuminated regions that would not overlap), there are triple lobe patterns in each case. Again, when there is no polarization, the measurement shows saturation.

4.2.4 $d = 190\,\mathrm{nm}$

The measurement of the $d = 190\,\mathrm{nm}$ array given in Fig. 4.13 is the first where the related spectral measurement showed no bright mode. The figures with no polarization and 0° seem to support this. There is no visible bending of the fringes and the center is unilluminated. This raises interest in the 90° and 135° and especially the 45° measurements where no bright mode should exist yet there is a distinct bright

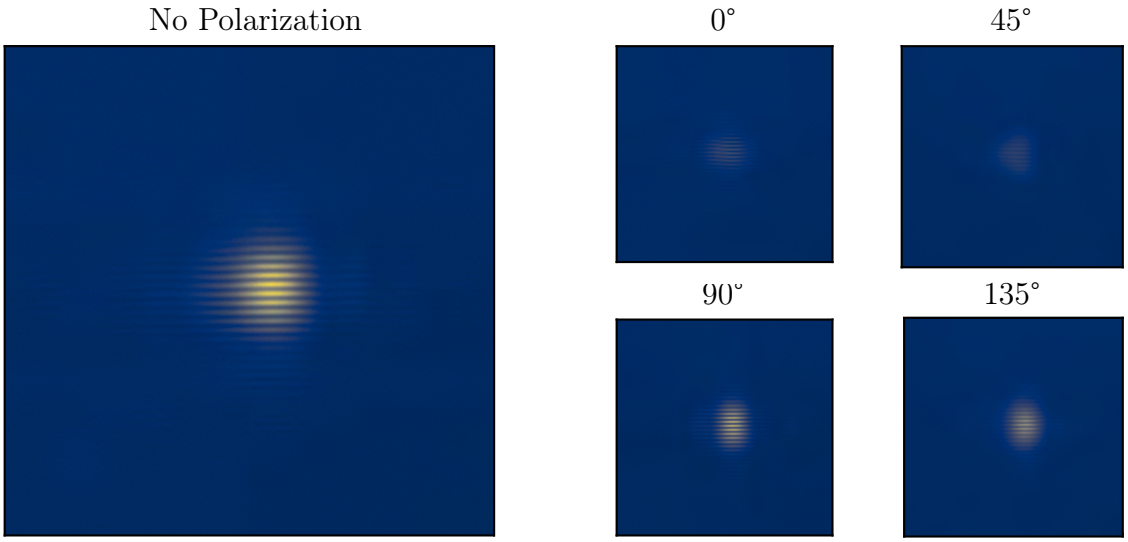

Figure 4.10: k-space interferometer measurements of the $d = 160\,\text{nm}$ array.

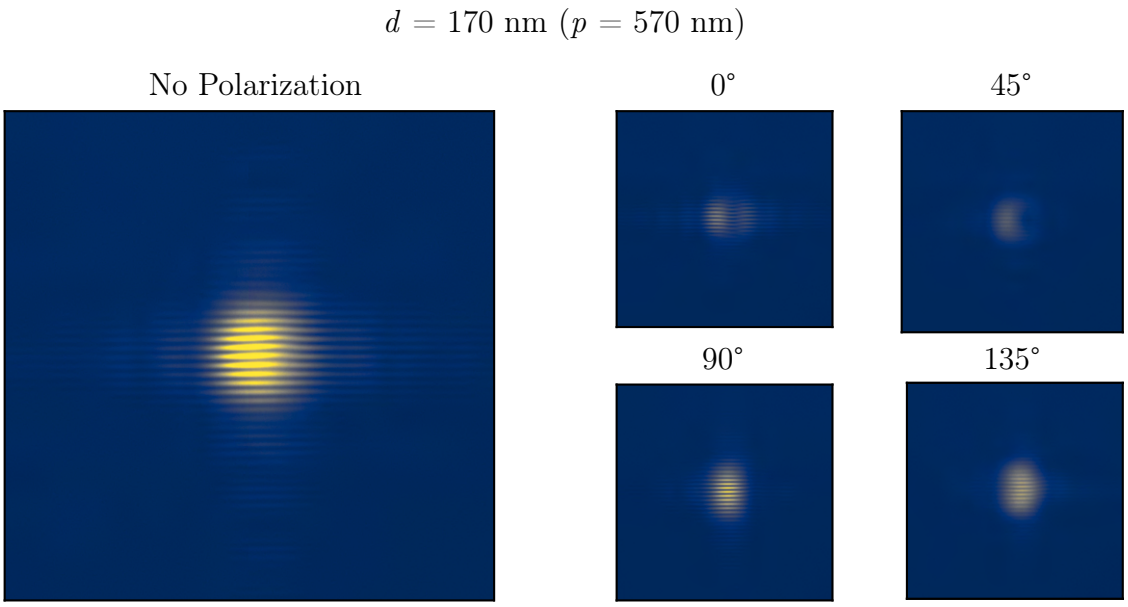

Figure 4.11: k-space interferometer measurements of the $d = 170\,\text{nm}$ array.

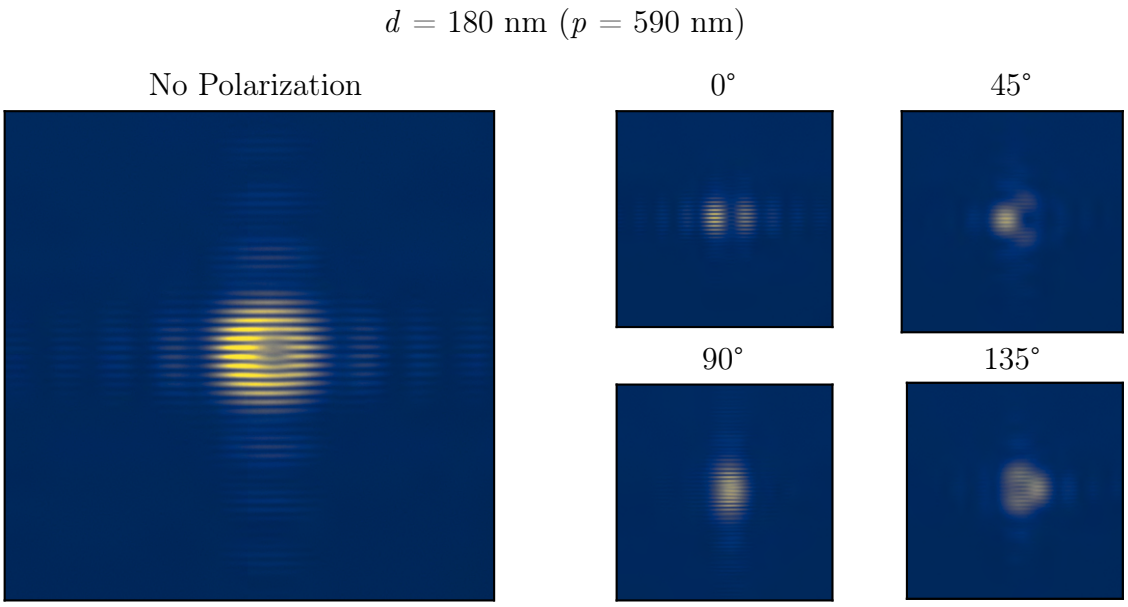

Figure 4.12: k-space interferometer measurements of the $d = 180\,\text{nm}$ array.

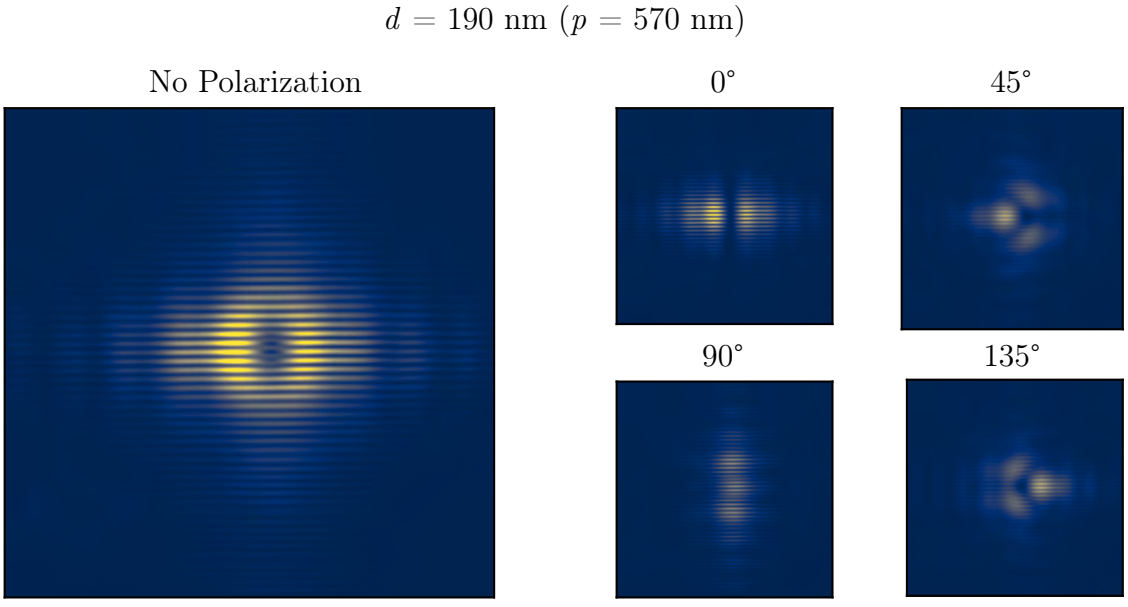

Figure 4.13: k-space interferometer measurements of the $d = 190\,\text{nm}$ array.

region at the center of the image. The 0° image is also over-saturated in this data set.

4.2.5 $d = 200\,\text{nm}$

Similar to the previous array, Fig. 4.14 has a clear LG_{01} shape when there is no polarizer. The 0° image also supports the intuition provided by the respective spectral measurement. The unexplained triple lobe pattern is still visible in the remaining cases, however. In this set of measurements, it appears that both the unpolarized and0° measurements are again saturated.

4.2.6 $d = 210\,\text{nm}$

The triple lobe pattern is again present in the 45°, 90° and 135° measurements of the $d = 210\,\text{nm}$ array in Fig. 4.15. The previous indicators of the bight mode are not visible at all here. There is, however, a small amount of fringe distortion in the top and bottom of the illuminated area visible in all of the measurements.

4.2.7 $d = 220\,\text{nm}$

Fig. 4.16 once again shows the three lobes, although here, in the 90° image the central lobe appears to be much less pronounced than the central lobe of the other images. Furthermore, all images appear to be more square than in measurements for the smaller arrays. The fringes are slightly more distorted in the top and bottom than in the previous array.

4.2.8 Analysis

The number of measurements that became oversaturated is disappointing, as it makes serious quantitative analysis of the fringes impossible here. It would be ideal to compare the peak fringe visibility of the measurements, however, in the situation that the image was saturated, not only is the data above the cutoff lost but there is bleed-over from the areas of constructive interference making the areas with destructive interference appear brighter. Thus, neither term in Eqn. 2.17 will be accurate. To better demonstrate this, Fig. 4.17 presents the central column of the 170 nm array without polarization. It is evident that some data has been lost from the constructive interference peaks.

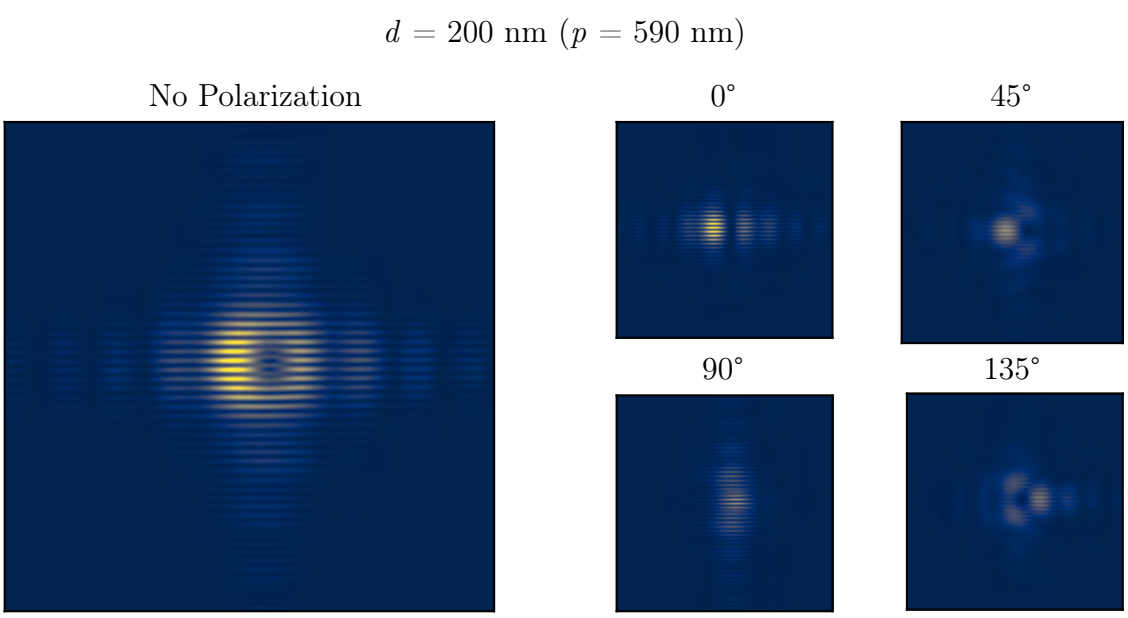

Figure 4.14: k-space interferometer measurements of the $d = 200\,\text{nm}$ array.

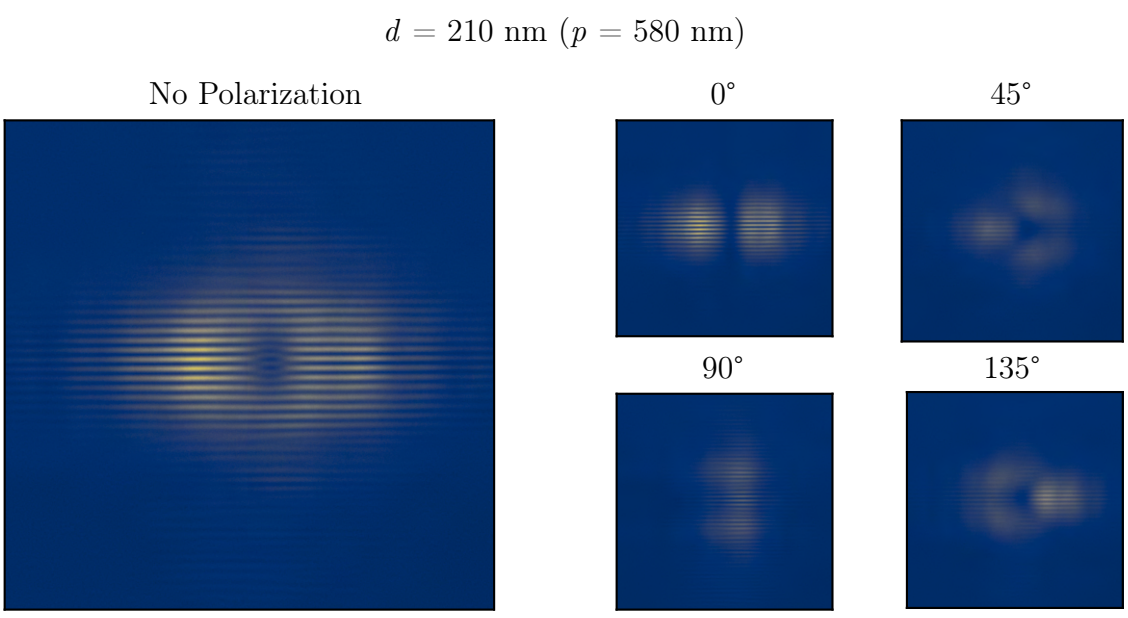

Figure 4.15: k-space interferometer measurements of the $d = 210\,\text{nm}$ array.

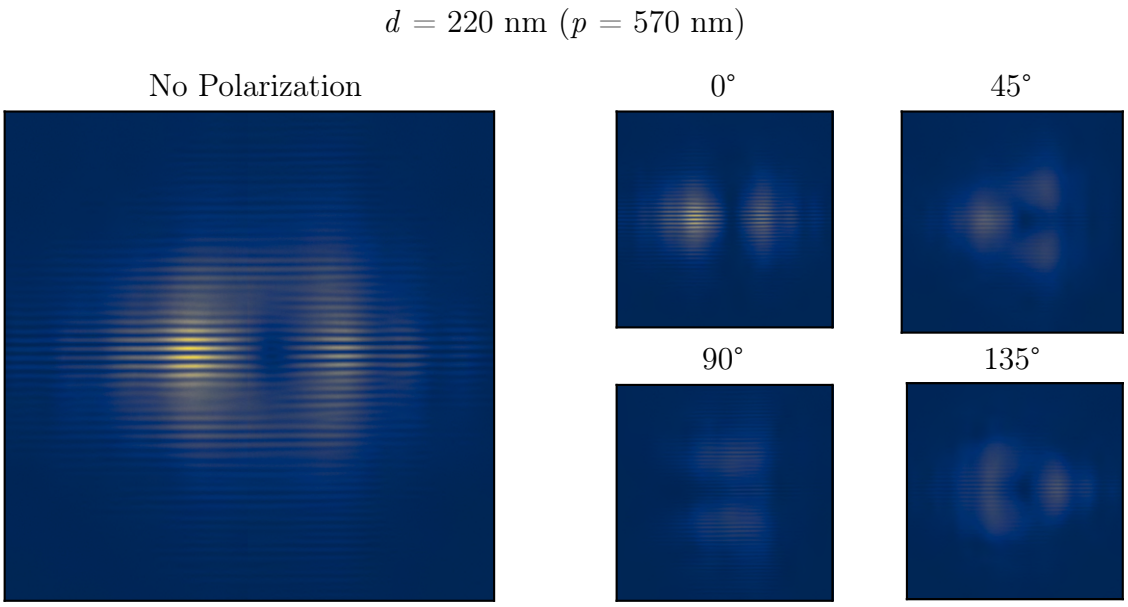

Figure 4.16: k-space interferometer measurements of the $d = 220\,\text{nm}$ array.

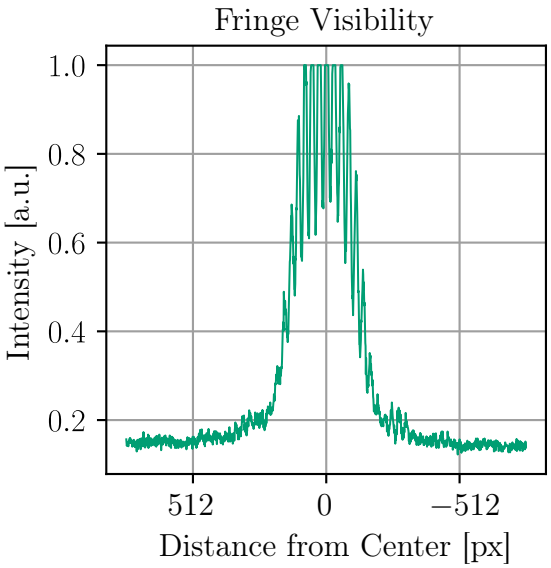

Figure 4.17: One column from the no-polarization image of the 170 nm array in Fig. 4.11 demonstrating saturation in the measurement.

Another concern in the k-space interferometry measurements is the triple lobe pattern. Fortunately, the fact that it is visible for all arrays which show a prominent dark mode, this provides a clue that the problem is systematic. One hypothesis for

the source of this issue is that there is a sort of shifting that is happening when the two fields are overlapped. Unfortunately, the one-way data was discarded after normalization in data processing to reduce computing time, and therefore no image of the field with only one arm open could be recovered. A suggested solution for recovering the data was to process the measurements with an experimental MATLAB script which relied heavily on Fourier transforms to simulate a simple superposition of the field coming from both arms. A second solution was presented by the data from Roman Calpe, who had recorded a one-way k-space measurement of the same 190 nm array under 45° polarization at a later time. By taking Roman Calpe's measurement and flipping it, it was possible to estimate how the fields from the two arms may have looked like for various alignments in the overlap. A result of both tests is given for comparison in Fig. 4.18, and seems to point to an offset existing in the measurements to be a plausible explanation of the triple lobe pattern.

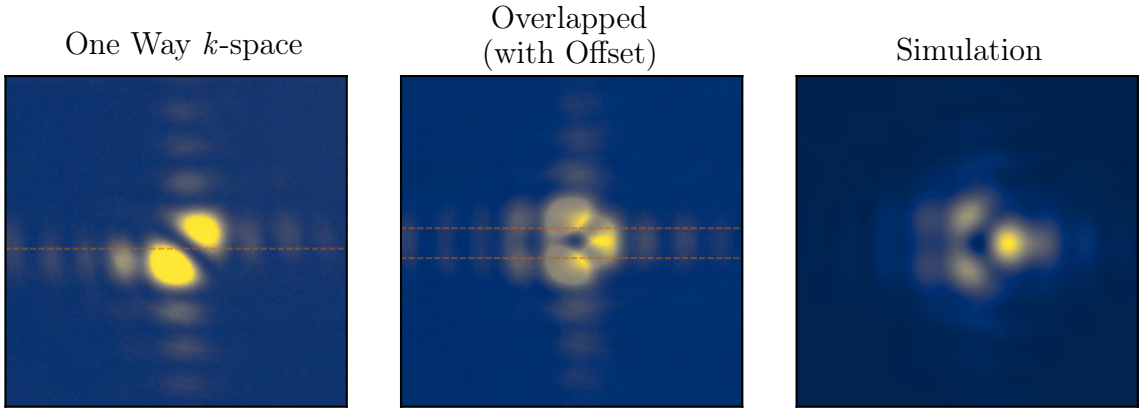

Figure 4.18: Investigations into the triple lobe patterns seen in the measured data. The orange line represents the middle of the fields, and illustrates how an offset between them could be the cause of the pattern.

A Further hindrance of these measurements is, given that WFI-2 only mirrors the field about a horizontal axis, it is impossible for the recorded measurements to fully reveal which BICs exist in the arrays on their own regardless of if there were an offset or if the fields had been perfectly aligned. This is a result of the light entering the interferometer after the analyzer. In other words, the vertical rotation means that the identifying components in the 45° and 135° cases cannot align in a way that is unique. It is however still possible to determine if the modes are TE or

TM by looking at the 0° and 90° measurements. Aside from the 160 nm array where the bright mode was too dominant to make any determination of the state of the dark mode, the results of this analysis are given in Table 4.3, and reiterate that the BIC type is the same for all arrays.

Array	Visible Regions				Proposed BIC
	0°	45°	90°	135°	
160 nm	N/A	N/A	N/A	N/A	N/A
170 nm	··	N/A	:	N/A	TE
180 nm	··	N/A	:	N/A	TE
190 nm	··	N/A	:	N/A	TE
200 nm	··	N/A	:	N/A	TE
210 nm	··	N/A	:	N/A	TE
220 nm	··	N/A	:	N/A	TE

Table 4.3: Proposed BICs of the modes based on analysis of k-space interferomentry measurements.

4.3 Real-space Interferometer Measurements

The real-space measurements were taken by the mirror-based WFI-1, and as the field has been flipped along both the x and y axes, the measurements represent the full spatial coherence of the field. As should be expected, the real-space images of the arrays show the square shape of the arrays. Because these are again interferometry measurements, the observation of fringes and where they are is important. Like previously, with the k-space measurements, the data has been processed by following the Fourier transform method, and as all data are normalized to the corresponding measurements, the colorbars are not included. Similarly, the area of interest is the same 1534×1534 pixels, meaning that the measurements or 5.2923 mm aside. Again, considering the direction of the beam, the images have been flipped to maintain consistency with the previous measurements.

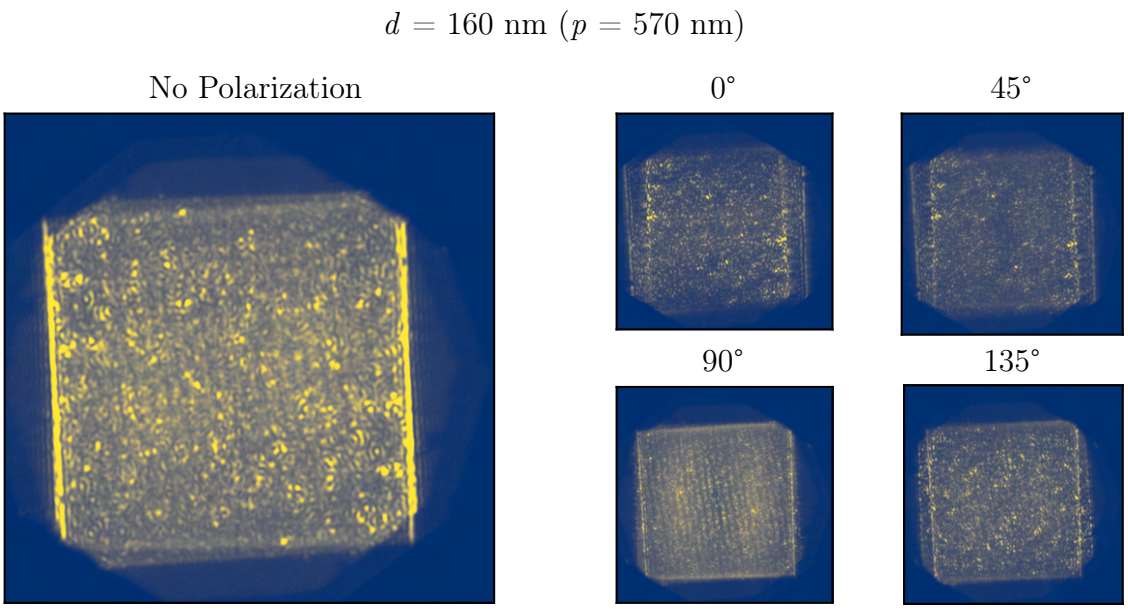

Figure 4.19: Real-space interferometer measurements of the $d = 160\,\text{nm}$ array.

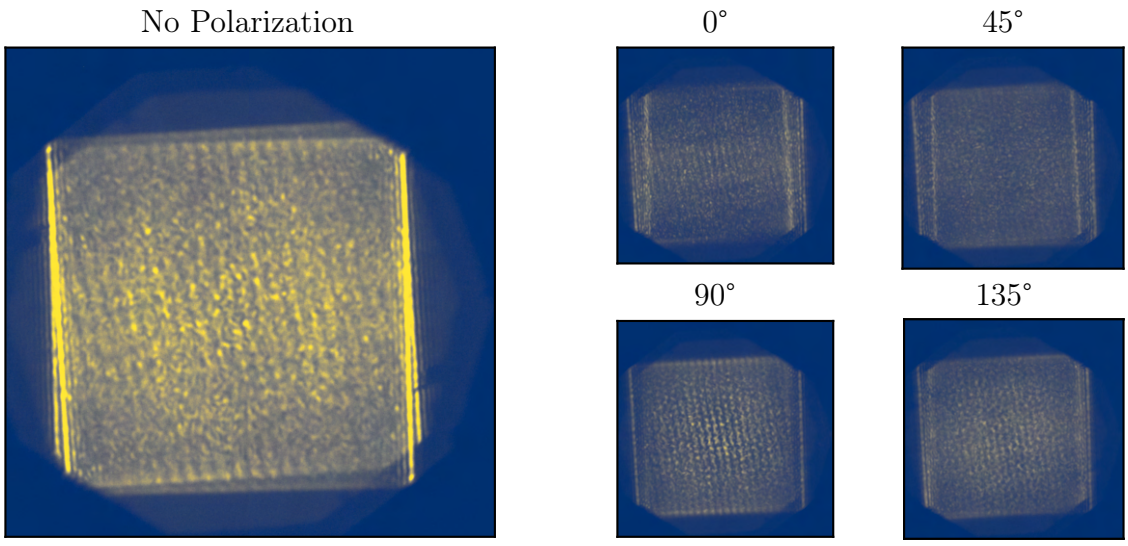

Figure 4.20: Real-space interferometer measurements of the $d = 170\,\text{nm}$ array.

4.3.1 $d = 160\,\mathrm{nm}$

The real-space spatial coherence of the field coming from the 160 nm array is given by Fig. 4.19. Fringes are seen in all images, but are most prominent for the 90° case. Of the polarized images, it is also the brightest.

4.3.2 $d = 170\,\mathrm{nm}$

In Fig. 4.20 the fringes have become more prominent in all cases, but are still clearest in the 90° measurement. Moreover, note that the center of the array is brighter than the edges.

4.3.3 $d = 180\,\mathrm{nm}$

The previous k-space measurements have shown that this array supports a roughly equally intense bright and dark mode. Observations of Fig. 4.21 show that the fringes are visible across the entire array for all measurements, but areas of darkness at certain locations of the array are starting to appear. This array also seems to have a defect in one of the corners.

4.3.4 $d = 190\,\mathrm{nm}$

Fig. 4.22 shows that there is a high level of coherence around the edges. The analyzer definitely seems to be filtering light from distinct regions. These dark regions are corresponding to the same regions as in the k-space interferometry and spectrometer measurements seen previously.

4.3.5 $d = 200\,\mathrm{nm}$

The unpolarized image of Fig. 4.23 has many of the same features as were seen in the previous array. The fringes are brightest around the edges, but overall they are dimmer. A defect is again present in a corner and is of course repeated to the opposite corner. The same pattern of dark regions persists.

4.3.6 $d = 210\,\mathrm{nm}$

In Fig. 4.24 the fringes are much less pronounced, and almost nonexistent in the 90°. The left and right edges of the array are indeed quite visible.

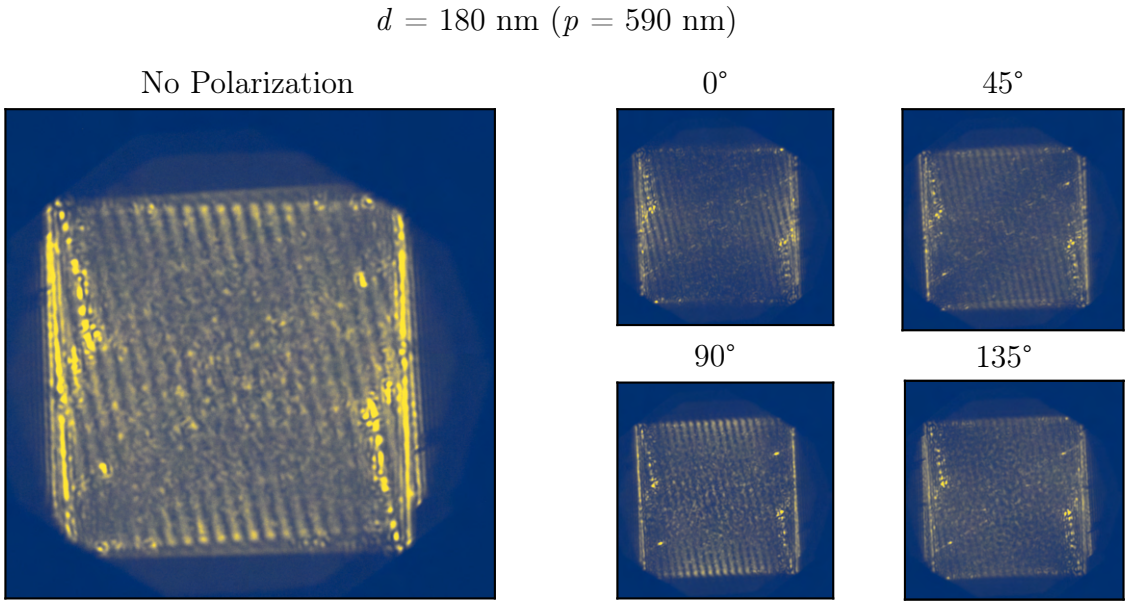

Figure 4.21: Real-space interferometer measurements of the $d = 180\,\text{nm}$ array.

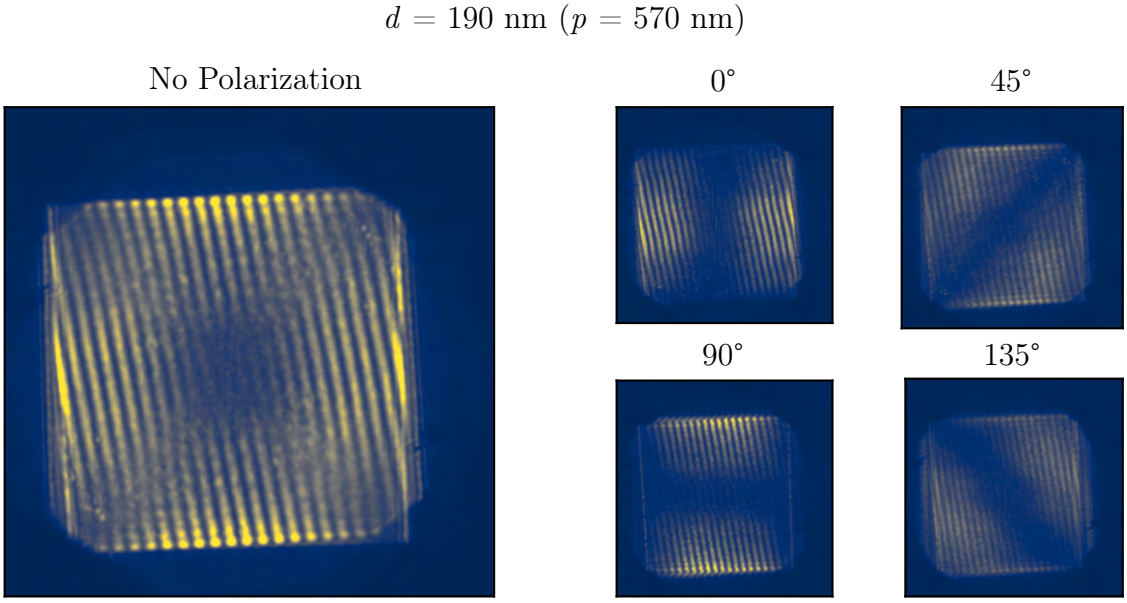

Figure 4.22: Real-space interferometer measurements of the $d = 190\,\text{nm}$ array.

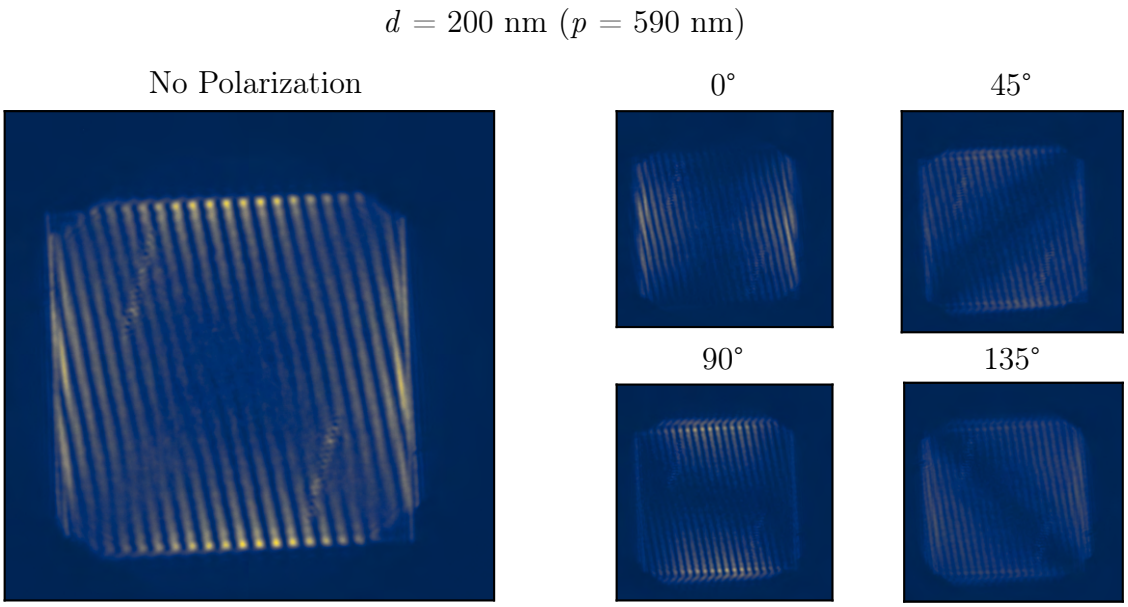

Figure 4.23: Real-space interferometer measurements of the $d = 200\,\text{nm}$ array.

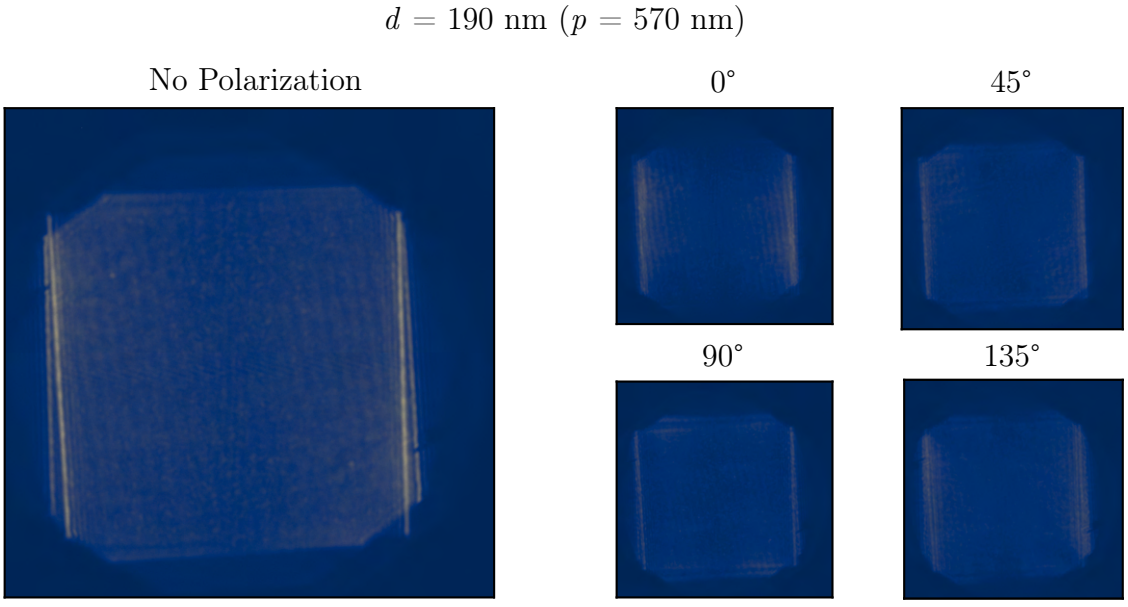

Figure 4.24: Real-space interferometer measurements of the $d = 210\,\text{nm}$ array.

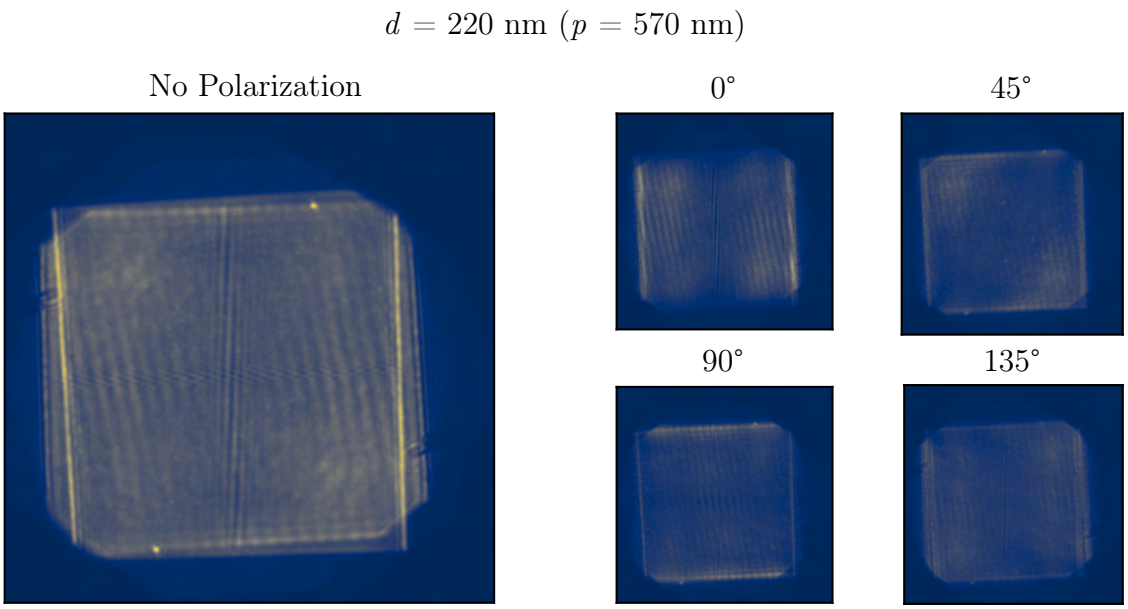

Figure 4.25: Real-space interferometer measurements of the $d = 220\,\text{nm}$ array.

4.3.7 $d = 220\,\text{nm}$

The measurement of the 220 nm array in Fig. 4.25 have two fringe patterns which have yet to be observed. Aside from the wide fringes which appear similar to those seen in the other arrays, there is a vertical region with more tightly packed fringes, and further, there is a horizontal region with even more tightly packed fringes. The cause for this is undetermined, however, it is known that this must relate to higher frequency light. As such, it may be a result of the pump beam being reflected by the large diameter particles, or the possibility exists that it is from some higher-order mode.

4.3.8 Analysis

Previous work in analyzing the origin of modes infinite lattice structures has shown that the bright mode radiates from the center of the array and the dark mode radiates from the edges [5]. This follows from the evolution of the modes from the plasmon resonances and is an effect that is clearly visible in the data. Having already identified the bright mode's dominance in the 160 nm array with the k-space measurements, it is clear that in the real space measurements of this array the overall intensity diminishes some towards the edge. Using the 190 nm array as an example

for a dark mode dominant array, it is very clear that the intensity is decreased in the center and is higher around the edges. In an attempt to demonstrate this progression, a new script was developed to calculate fringes in a given region. For the bright modes an area just off-center (to avoid the unknown phenomenon at the center in the 220 nm array) was used, and for the dark modes an estimate of peak fringe visibility was used to establish the region. The results of this analysis for the

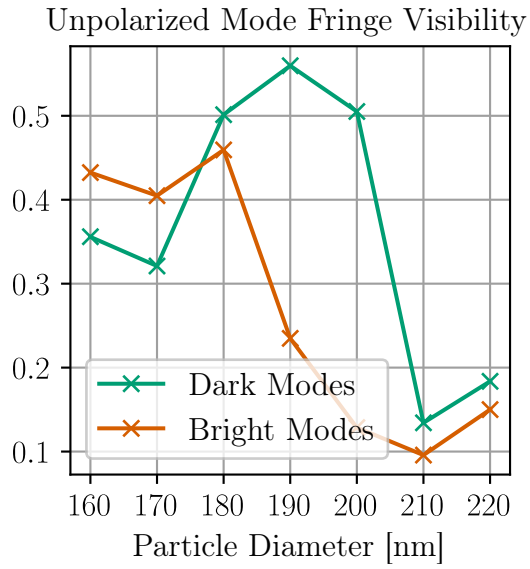

Figure 4.26: Fringe visibility by mode in unpolarized measurements.

unpolarized measurements are presented in Fig. 4.26. The trend seen here is not overly dissimilar to that seen in Fig. 4.8b where both plots show a similar change in the dominance of the bright mode somewhere between 170 nm and 180 nm.

Looking at the measurements collected with the analyzer in provides the final evidence for identifying which BIC is present in each of the arrays. Unfortunately, the bright mode is too dominant in the 160 nm. and 170 nm arrays to make reasonable judgments for this. Similar to before, the illuminated areas are noted in Table 4.4. It is now know that the BICs which have been predicted using the dark mode seem to be the ones which are present in the arrays. It is worth reiterating that there was no requirement that all seven arrays have the same BIC. Close tuning of the parameters has shown that any of the four options may be produced by similar situations to those used here.

Array	Visible Regions				Fundamental BIC
	0°	45°	90°	135°	
160 nm	N/A	N/A	N/A	N/A	N/A
170 nm	N/A	N/A	N/A	N/A	N/A
180 nm	∵	∴	:	∴	TE-1
190 nm	∵	∴	:	∴	TE-1
200 nm	∵	∴	:	∴	TE-1
210 nm	∵	N/A	N/A	N/A	TE
220 nm	∵	∴	:	∴	TE-1

Table 4.4: BICs of the modes based on analysis of real space interferomentry measurements.

Chapter V

Conclusions

In this thesis, I have presented in detail the key theories governing the plasmonic nanolaser as well as the methods for testing the polarization and lasing capabilities of the laser. In addition, I have discussed the theories governing both the laser and the measurements in detail. Each of the seven arrays tested has been measured under five different polarization states by a spectrometer, and two different wavefront folding interferometers giving real space and k-space coherence for a total of 105 measurements. My examination of the data revealed that in the far field, all arrays are capable of producing a recognizable toroidal dark mode which resembles an LG_{01} mode, with the three smaller arrays also producing a bright mode which resembles the LG_{00} mode as well. A bright mode dominant regime was found to exist in arrays with a particle diameter less than 170 nm, changing to a dark mode dominant regime taking over when the particle diameter is greater than 180 nm. In connection to this, I found that the intensity of the dark mode increases exponentially across the measured arrays as the diameter of the particles increases. In investigating the polarization, I discovered that the bright mode is linearly polarized with the calculated degree of linear polarization at 0.974 on the low end and a maximum of 0.999 found for the 170 nm array. For the dark mode, I was able to use the polarization of the k-space to establish that of the four possibilities, TE-1 is the bound state in continuum for all arrays. Simple analysis of the spectrum revealed a drifting of the beam's wavelength as the diameter increased which does not follow the current model. Lastly, I was able to compare the real space and k- space measurements to demonstrate the evolution of the bright and dark modes of the lattice.

Developing the plasmonic nanolaser does face some obstacles, but there is no

lack of applications to motivate continued efforts, and the future avenues of research include measuring the Stokes parameters for the entire beam in the near and far field which is likely to help further identify the evolution of the modes, and help establish better if other modes may present, and possibly help improve the model for predicting the emitted wavelength, particularly for the dark modes. Investigating more lattices such as those with geometries around that of the 180 nm array to further identify the change in mode dominance, as well as larger diameter arrays to better understand the evolution of intensity observed in the dark mode. All of these would improve the general understanding of not just this plasmonic nanolaser, but many others as well.

References

[1] S. Azzam, A. Kildishev, R.-M. Ma, C.-Z. Ning, R. Oulton, V. Shalaev, M. Stockman, J.-L. Xu, and X. Zhang, "Ten years of spasers and plasmonic nanolasers," *Light: Science & Applications* **9**, 90 (2020).

[2] R.-M. Ma and R. Oulton, "Applications of nanolasers," *Nature Nanotechnology* **14**, 12–22 (2018).

[3] R.-M. Ma, X. Yin, R. F. Oulton, V. J. Sorger, and X. Zhang, "Multiplexed and Electrically Modulated Plasmon Laser Circuit," *Nano Letters* **12**, 5396–5402 (2012), PMID: 22989288.

[4] S. Wang, B. Li, X.-Y. Wang, H.-Z. Chen, Y.-L. Wang, X.-W. Zhang, L. Dai, and R.-M. Ma, "High-Yield Plasmonic Nanolasers with Superior Stability for Sensing in Aqueous Solution," *ACS Photonics* **4**, 1355–1360 (2017).

[5] T. Hakala, H. Rekola, A. Väkeväinen, J. Martikainen, M. Nečada, A. Moilanen, and P. Törmä, "Lasing in dark and bright modes of a finite-sized plasmonic lattice," *Nature Communications* **8**, 1–7 (2017), | openaire: EC/FP7/340748/EU//CODE.

[6] A. M. Yao and M. J. Padgett, "Orbital angular momentum: origins, behavior and applications," *Adv. Opt. Photon.* **3**, 161–204 (2011).

[7] V. Lerner, D. Shwa, Y. Drori, and N. Katz, "Shaping Laguerre–Gaussian laser modes with binary gratings using a digital micromirror device," *Opt. Lett.* **37**, 4826–4828 (2012).

[8] J. P. Torres, Y. Deyanova, L. Torner, and G. Molina-Terriza, "Preparation of engineered two-photon entangled states for multidimensional quantum information," *Phys. Rev. A* **67**, 052313 (2003).

[9] M. Koba and P. Szczepanski, "Coupled Mode Theory of Photonic Crystal Lasers," Chap 14 in *Photonic Crystals*, A. Massaro, ed. (IntechOpen, Rijeka, 2012).

[10] J.-K. Yang, M. J. Rooks, S. Boriskina, G. Solomon, L. D. Negro, and H. Cao, "Lasing from Localized Modes in Deterministic Aperiodic Nanostructures," in *Conference on Lasers and Electro-Optics 2010* (2010), p. QTuF2.

[11] C. Kittel, *Introduction to Solid State Physics* (Wiley, 2004).

[12] Y. Pan, L. Chu, J. Liu, B. Lv, L. A. Belfiore, and J. Tang, "Precise Control of Copper-Localized Surface Plasmon Resonance in the Near Infrared Region for Enhancement of Up-Conversion Luminescence," *Metals* **10** (2020).

[13] J. M. Taskinen, A. J. Moilanen, H. Rekola, K. Kuntze, A. Priimagi, P. Törmä, and T. K. Hakala, "All-Optical Emission Control and Lasing in Plasmonic Lattices," *ACS Photonics* **7**, 2850–2858 (2020).

[14] R. Heilmann, A. I. Väkeväinen, J.-P. Martikainen, and P. Törmä, "Strong coupling between organic dye molecules and lattice modes of a dielectric nanoparticle array," *Nanophotonics* **9**, 267–276 (2020).

[15] V. G. Kravets, F. Schedin, and A. N. Grigorenko, "Extremely Narrow Plasmon Resonances Based on Diffraction Coupling of Localized Plasmons in Arrays of Metallic Nanoparticles," *Phys. Rev. Lett.* **101**, 087403 (2008).

[16] B. Stein, J.-Y. Laluet, E. Devaux, C. Genet, and T. W. Ebbesen, "Surface Plasmon Mode Steering and Negative Refraction," *Phys. Rev. Lett.* **105**, 266804 (2010).

[17] B. Stein, E. Devaux, C. Genet, and T. W. Ebbesen, "Self-collimation of surface plasmon beams," *Opt. Lett.* **37**, 1916–1918 (2012).

[18] F. van Beijnum, P. J. van Veldhoven, E. J. Geluk, M. J. A. de Dood, G. W. 't Hooft, and M. P. van Exter, "Surface Plasmon Lasing Observed in Metal Hole Arrays," *Phys. Rev. Lett.* **110**, 206802 (2013).

[19] A. H. Schokker and A. F. Koenderink, "Lasing at the band edges of plasmonic lattices," *Phys. Rev. B* **90**, 155452 (2014).

[20] L. Langguth, A. H. Schokker, K. Guo, and A. F. Koenderink, "Plasmonic phase-gradient metasurface for spontaneous emission control," *Phys. Rev. B* **92**, 205401 (2015).

[21] D. K. G. de Boer, M. A. Verschuuren, K. Guo, A. F. Koenderink, J. G. Rivas, and S. R.-K. Rodriguez, "Directional sideward emission from luminescent plasmonic nanostructures," *Opt. Express* **24**, A388–A396 (2016).

[22] D. Canneson, E. L. Moal, S. Cao, X. Quélin, H. Dallaporta, G. Dujardin, and E. Boer-Duchemin, "Surface plasmon polariton beams from an electrically excited plasmonic crystal," *Opt. Express* **24**, 26186–26200 (2016).

[23] J.-F. Bryche, G. Barbillon, B. Bartenlian, G. Dujardin, E. Boer-Duchemin, and E. Le Moal, "k-space optical microscopy of nanoparticle arrays: Opportunities and artifacts," *Journal of Applied Physics* **124**, 043102 (2018).

[24] S. Mohamed, J. Wang, H. Rekola, J. Heikkinen, B. Asamoah, L. Shi, and T. K. Hakala, "Topological charge engineering in lasing bound states in continuum," (2020), 2012.15642.

[25] E. Hecht, *Optics; Global Edition*, 5th ed. (Pearson Education Limited, Essex, England, 2017).

[26] M. H. Madsen, P. Boher, P.-E. Hansen, and J. F. Jørgensen, "Alignment-free characterization of 2D gratings," *Appl. Opt.* **55**, 317–322 (2016).

[27] R. Mezrich, "A perspective on K-space.," *Radiology* **195**, 297–315 (1995), PMID: 7724743.

[28] B. Saleh and M. Teich, *Fundamentals of Photonics, 3rd Edition* (John Wiley & Sons, Inc., 2019).

[29] S. Wilk, "Edible lasers: What's the next course?," *Optics and Photonics News* **20**, 14–15 (2009).

[30] Z. Su, N. Li, E. S. Magden, M. Byrd, Purnawirman, T. N. Adam, G. Leake, D. Coolbaugh, J. D. B. Bradley, and M. R. Watts, "Ultra-compact and low-threshold thulium microcavity lasermonolithically integrated on silicon," *Opt. Lett.* **41**, 5708–5711 (2016).

[31] O. Svelto, *Principles of Lasers* (Springer Science+Business Media, LLC, 2010).

[32] C. Deeb and J.-L. Pelouard, "Plasmon lasers: coherent nanoscopic light sources," *Phys. Chem. Chem. Phys.* **19**, 29731–29741 (2017).

[33] M. Born and E. Wolf, *Principles of Optics: 60th Anniversary Edition* (Cambridge University Press, 2019).

[34] R. Whalen, "Wavefront Folding Interferometer," (1966).

[35] A. Halder, H. Partanen, A. Leinonen, M. Koivurova, T. K. Hakala, T. Setälä, J. Turunen, and A. T. Friberg, "Mirror-based scanning wavefront-folding interferometer for coherence measurements," *Opt. Lett.* **45**, 4260–4263 (2020).

[36] W. W. Macy, "Two-dimensional fringe-pattern analysis," *Appl. Opt.* **22**, 3898–3901 (1983).

[37] G. Reid, "Automatic fringe pattern analysis: A review," *Optics and Lasers in Engineering* **7**, 37–68 (1986).

[38] M. Takeda, H. Ina, and S. Kobayashi, "Fourier-transform method of fringe-pattern analysis for computer-based topography and interferometry," *J. Opt. Soc. Am.* **72**, 156–160 (1982).

[39] M. Bandres and J. Gutierrez Vega, "Ince-Gaussian beams," *Optics letters* **29**, 144–6 (2004).

[40] B. Zhang, J. Zerubia, and J.-C. Olivo-Marin, "Gaussian approximations of fluorescence microscope point-spread function models," *Appl. Opt.* **46**, 1819–1829 (2007).

[41] Q. Zhan, "Cylindrical vector beams: from mathematical concepts to applications," *Adv. Opt. Photon.* **1**, 1–57 (2009).

[42] M. Padgett and L. Allen, "Light with a twist in its tail," *Contemporary Physics* **41**, 275–285 (2000).

[43] T. Setälä, A. Shevchenko, M. Kaivola, and A. T. Friberg, "Degree of polarization for optical near fields," *Phys. Rev. E* **66**, 016615 (2002).

[44] E. Zubko and E. Chornaya, "On the Ambiguous Definition of the Degree of Linear Polarization," *Research Notes of the AAS* **3** (2019).

[45] L. Li, Z. Li, K. Li, L. Blarel, and M. Wendisch, "A method to calculate Stokes parameters and angle of polarization of skylight from polarized CIMEL sun/sky radiometers," *Journal of Quantitative Spectroscopy and Radiative Transfer* **149**, 334–346 (2014).

[46] F. Goudail and A. Bénière, "Estimation precision of the degree of linear polarization and of the angle of polarization in the presence of different sources of noise," *Applied optics* **49**, 683–93 (2010).

[47] P. Törmä and W. L. Barnes, "Strong coupling between surface plasmon polaritons and emitters: a review," *Reports on Progress in Physics* **78**, 013901 (2014).

[48] H. Raether, *Surface Plasmons on Smooth and Rough Surfaces and on Gratings* (Springer Berlin Heidelberg, Berlin, Heidelberg, 1988).

[49] A. Kodigala, T. Lepetit, Q. Gu, B. Bahari, Y. Fainman, and B. Kanté, "Lasing action from photonic bound states in continuum," *Nature* **541**, 196–199 (2017).

[50] C. W. Hsu, B. Zhen, A. Stone, J. Joannopoulos, and M. Soljačić, "Bound states in the continuum," *Nature Reviews Materials* **1**, 16048 (2016).

[51] Photonics Solutions, "Quantronix Integra-C 3.5," (2004), https://www.photonicsolutions.co.uk/upfiles/QXIntegra-C.pdf.

[52] FLIR, "Grasshopper 3 GS3–U3–32S4M–C," (2017), https://flir.app.boxcn.net/s/859w5hl6yv25yo4c5aqvdnl2ask34n4i/file/418656969139.

[53] Andor, "Kymera 193i," (2021), https://andor.oxinst.com/assets/uploads/products/andor/documents/andor-kymera-193-specifications.pdf.

[54] Andor, "Newton EMCCD DU970P," (2021), https://andor.oxinst.com/assets/uploads/products/andor/documents/andor-newton-emccd-specifications.pdf.

[55] Schrödinger, LLC, "The PyMOL Molecular Graphics System, Version 2.4," (2020).

[56] L.-P. Leppänen, K. Saastamoinen, A. T. Friberg, and T. Setälä, "Measurement of the degree of temporal coherence of unpolarized light beams," *Photon. Res.* **5**, 156–161 (2017).